

This article is a companion to Griffin et al. (2022), <https://doi.org/10.1029/2021JE007080>

Key Points:

- Electron backscatter diffraction reveals shock-derived deformation to mask nonshock deformation even in low deformation regions in the nakhlites
- Intracrystalline misorientation patterns indicate nine distinct derived deformation signatures for 16 nakhlites
- Intracrystalline misorientation patterns are identified within low deformation regions interpreted as emplacement deformation

Supporting Information:

Supporting Information may be found in the online version of this article.

Correspondence to:

S. Griffin,
Sammy.Griffin@glasgow.ac.uk

Citation:

Griffin, S., Daly, L., Piazzolo, S., Forman, L. V., Cohen, B. E., Lee, M. R., et al. (2022). Can the magmatic conditions of the Martian nakhlites be discerned via investigation of clinopyroxene and olivine intracrystalline misorientations? *Journal of Geophysical Research: Planets*, 127, e2021JE007082. <https://doi.org/10.1029/2021JE007082>

Received 2 OCT 2021
Accepted 30 MAR 2022




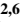


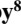

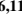
Author Contributions:

Conceptualization: S. Griffin, L. Daly
Data curation: S. Griffin
Formal analysis: S. Griffin, L. Daly, L. V. Forman, P. W. Trimby, R. J. Baumgartner, G. K. Benedix
Funding acquisition: M. R. Lee
Investigation: S. Griffin
Methodology: S. Griffin, L. Daly

© 2022. The Authors.

This is an open access article under the terms of the [Creative Commons Attribution License](https://creativecommons.org/licenses/by/4.0/), which permits use, distribution and reproduction in any medium, provided the original work is properly cited.

Can the Magmatic Conditions of the Martian Nakhlites be Discerned via Investigation of Clinopyroxene and Olivine Intracrystalline Misorientations?

S. Griffin¹ , L. Daly^{1,2,3,4} , S. Piazzolo⁵ , L. V. Forman^{2,6} , B. E. Cohen⁷ , M. R. Lee¹ , P. W. Trimby⁸ , R. J. Baumgartner^{9,10} , G. K. Benedix^{2,6,11} , and B. Hoefnagels¹²

¹School of Geographical and Earth Sciences, University of Glasgow, Glasgow, UK, ²Space Science and Technology Centre, School of Earth and Planetary Sciences, Curtin University, Perth, WA, Australia, ³Australian Centre for Microscopy and Microanalysis, The University of Sydney, Sydney, NSW, Australia, ⁴Department of Materials, University of Oxford, Oxford, UK, ⁵School of Earth and Environment, University of Leeds, Leeds, UK, ⁶Department of Earth and Planetary Sciences, Western Australia Museum, Perth, WA, Australia, ⁷School of Geosciences, University of Edinburgh, Edinburgh, UK, ⁸Oxford Instruments Nano Analysis, High Wycombe, UK, ⁹School of Biological, Earth and Environmental Sciences, The University of New South Wales, Kensington, NSW, Australia, ¹⁰CSIRO Mineral Resources, Australian Resources Research Centre, Kensington, NSW, Australia, ¹¹Planetary Science Institute, Houston, TX, USA, ¹²Big Bang Meteorites

Abstract Deformation is a near ubiquitous process that is observed within nearly all naturally forming rocks. Electron backscatter diffraction (EBSD) is a technique that enables slip-systems (a form of plastic deformation) to be inferred from intracrystalline misorientations at a comparable scale to the representative CPO analysis (≥ 300 crystals for the nakhlites). Extensive laboratory and studies on naturally occurring samples have identified preferential mantle condition extrinsic parameters for specific slip-system signatures within olivine and clinopyroxene. Intracrystalline misorientation patterns for olivine and augite (high Ca-clinopyroxene) for 16 different Martian nakhlite meteorites (21 sections) were analyzed and assessed against these known parameters. Investigation of high and low deformation regions within the nakhlites revealed a shift in intracrystalline misorientation patterns for 10 of the 21 sections. Interpreted as both shock (high deformations) and emplacement (low deformation) signatures, the observed variations in deformation patterns for the two main regimes of deformation indicate heterogeneous sampling of the nakhlite source crater. Our findings indicate that shock deformation is prevalent throughout the nakhlites, and that great care needs to be taken when interpreting intracrystalline misorientations of crystals within apparent lower deformation regions.

Plain Language Summary Clinopyroxene and olivine are important minerals for studying igneous processes on Mars and Earth (from the surface to the upper mantle). Here, clinopyroxene and olivine intracrystalline misorientation patterns—deformational movement within a crystal—were investigated in a group of meteorites from Mars using the specialist microscopic technique of electron backscatter diffraction (EBSD). The nakhlites are mafic rocks representing the largest collection of rocks from a singular—but as yet unknown—location on Mars. Combined intracrystalline misorientation patterns for both olivine and clinopyroxene reveal nine different shock deformation signatures for the nakhlites indicating that they were sourced from multiple locations within the ejection crater. Nonshock related deformation can also be observed but tends to be masked by the dominance of shock deformation features even in low deformation regions.

1. Introduction

Deformation within rocks is driven by a wide variety of geological processes for example, compaction (mountain building, subduction, burial), extension (rifting), shear (flow, faulting), and dramatic changes in both temperature (contact metamorphism, melting/recrystallization, hypervelocity impacts, and hydrothermal activity) and pressure (hypervelocity impacts, rapid burial). Extrinsic parameters presented over a rock's geological history will impact the way each crystal within the sample will grow and deform. Mineral deformation within rocks can occur via several mechanisms including elastic, brittle, and ductile deformation, where ductile deformation includes dislocation creep, diffusion creep, and dissolution-precipitation creep. Micro-structures and defects (*e.g.*, dislocations) present within a mineral's crystal lattice record important information pertaining to its crystal plastic deformation (Ashby, 1970, 1983; Fleck et al., 1994; Poirier, 1975, 1985, 1995; Poirier & Nicolas, 1975; Sciences, 1978; Stocker & Ashby, 1973). Plastic deformation is defined as a stress and/or strain-derived

Project Administration: S. Griffin, M. R. Lee
Resources: L. V. Forman, M. R. Lee, G. K. Benedix, B. Hoefnagels
Supervision: L. Daly, B. E. Cohen, M. R. Lee
Writing – original draft: S. Griffin
Writing – review & editing: S. Griffin, L. Daly, S. Piazzolo, L. V. Forman, B. E. Cohen, M. R. Lee, P. W. Trimby

permanent change lacking brittle failure or volume change within a material. Plastic deformation in rocks is typically accommodated at the nanometer scale by crystallographic slip or rotation. Crystallographic slip-systems are directional movement of either slip or rotation that occur around specific crystallographic axes within either the crystal lattice, subboundaries, or inequant crystals (Law, 1990). In geological specimens, plastic deformation has been shown to develop through either crystallization processes for example, mantle/flow rheology, growth twins, (Cordier, 2002; Fei et al., 2012; Frets et al., 2012; Henry et al., 2017; Yao et al., 2019; Zhang et al., 2006) and/or subsequent modification processes for example, metamorphic shear, mineralogical dehydration/degassing, compaction, or shock (Friedrich et al., 2017; Godard & van Roermund, 1995; Ruzicka & Hugo, 2018; Tasaka et al., 2008; van Roermund & Boland, 1981; Yao et al., 2019). The accumulation of these deformation micro-structures, are reported for a given phase as crystallographic preferred orientation (CPO) also known as lattice preferred orientation (LPO) (Bernard et al., 2019; Hunter, 1996; Mainprice et al., 2015). When combined across a representative area of a rock, these micro-structures produce a macroscale pattern of plastic deformation.

Previous studies of crystallographic dislocations, have shown an activation dependence of slip around specific crystallographic axes, when a crystal is exposed to differential stress from varying extrinsic conditions for example, stress, strain, temperature, pressure, and water content (*e.g.*, Bernard et al., 2019; Katayama et al., 2004; Karato et al., 2008; Liu et al., 2019; Raterron & Jaoul, 1991; Raterron et al., 2011). Subsequently, through extensive laboratory experiments and studies of naturally occurring samples, the ability to broadly ascertain the environment (pressure, temperature, stress, strain, and water content) parameters a rock experienced during deformation has started to develop. These activation parameters therefore have the potential to provide insight into a given sample's geological history (Barber et al., 2010). However, despite the wealth of information that is stored within crystallographic dislocations and the ever-increasing body of the literature, there is a lot about these systems that are neither utilized nor fully understood.

Intrinsic controls (*e.g.*, chemistry) alongside extrinsic controls (*e.g.*, temperature, pressure, stress magnitude, and strain rate) have long been recognized as important factors for the activation of crystallographic slip-systems in minerals (Ashby, 1983; Barber et al., 2010; Bernard et al., 2019; Groves & Kelly, 1963; Jaoul & Raterron, 1994; Müller et al., 2008; Poirier, 1982; Woodward, 2005). However, recent studies of olivine have shown that there are additional factors that can also influence the activation of a given slip-system (Barber et al., 2010; Bernard et al., 2019). These factors include the mechanism of deformation, water content, deformation geometry, presence of melt, and previous deformation history (Boneh & Skemer, 2014; Hansen et al., 2014; H. Jung et al., 2006; Haemyeong Jung et al., 2009; Katayama & Karato, 2006; Précigout & Hirth, 2014; Qi et al., 2018; Sundberg & Cooper, 2008). These other identified factors have the capacity to shift the previously identified activation boundaries of specific slip-systems, related to the minerals' chemistry, and the local temperature, pressure, and time frame over which deformation occurs. This is why slip-systems observed in some naturally occurring samples show slip-system signatures at lower extrinsic values compared to those determined from laboratory experiments (Bernard et al., 2019).

Here the activation of crystallographic slip-systems within olivine and augite (high Ca-clinopyroxene; Figures 1 and 2), representatives of the orthorhombic and monoclinic crystal systems, respectively, are inferred from analysis of intra-crystalline misorientations. Olivine has been extensively studied, both experimentally and in naturally occurring samples of mantle rocks (Bernard et al., 2019; Kaboli et al., 2017; Li et al., 2020; Mainprice et al., 2005; Mei & Kohlstedt, 2000; Poirier, 1975; Soustelle & Manthilake, 2017). Thus, the activation criteria for olivine's crystallographic slip-systems over a variety of parameters are fairly well constrained (Bernard et al., 2019; Karato et al., 2008; Katayama & Karato, 2006). Augite, on the other hand, is only starting to be studied in the same level of detail (Tedonkenfack et al., 2021; Van der Werf et al., 2017). Previous work exploring slip-systems in clinopyroxene has predominantly focused on diopside (monoclinic with a similar crystal lattice structure to augite), but mostly in laboratory settings (Bascou et al., 2002; Bystricky & Mackwell, 2001; Ingrin et al., 1991; Jaoul & Raterron, 1994; Mauler et al., 2000; Skrotzki, 1994), where many of these crystallographic slip-systems have yet to be observed within naturally occurring rocks (Keppler, 2018; Skrotzki, 1994; Tedonkenfack et al., 2021; Van der Werf et al., 2017). Current knowledge of clinopyroxene crystallographic slip-system activation (often based off numerical simulations for example, Ulrich and Mainprice (2005)), shows strong dependence of crystal orientation relative to the principal stress axes. Observation of clinopyroxene indicate that the dominant slip-system signature pairing of dominant (100)[001] with minor (001)[100] (Figure 2) will form under most Earth-relevant extrinsic conditions (Kollé & Blacic, 1982; P. Raterron et al., 1994).

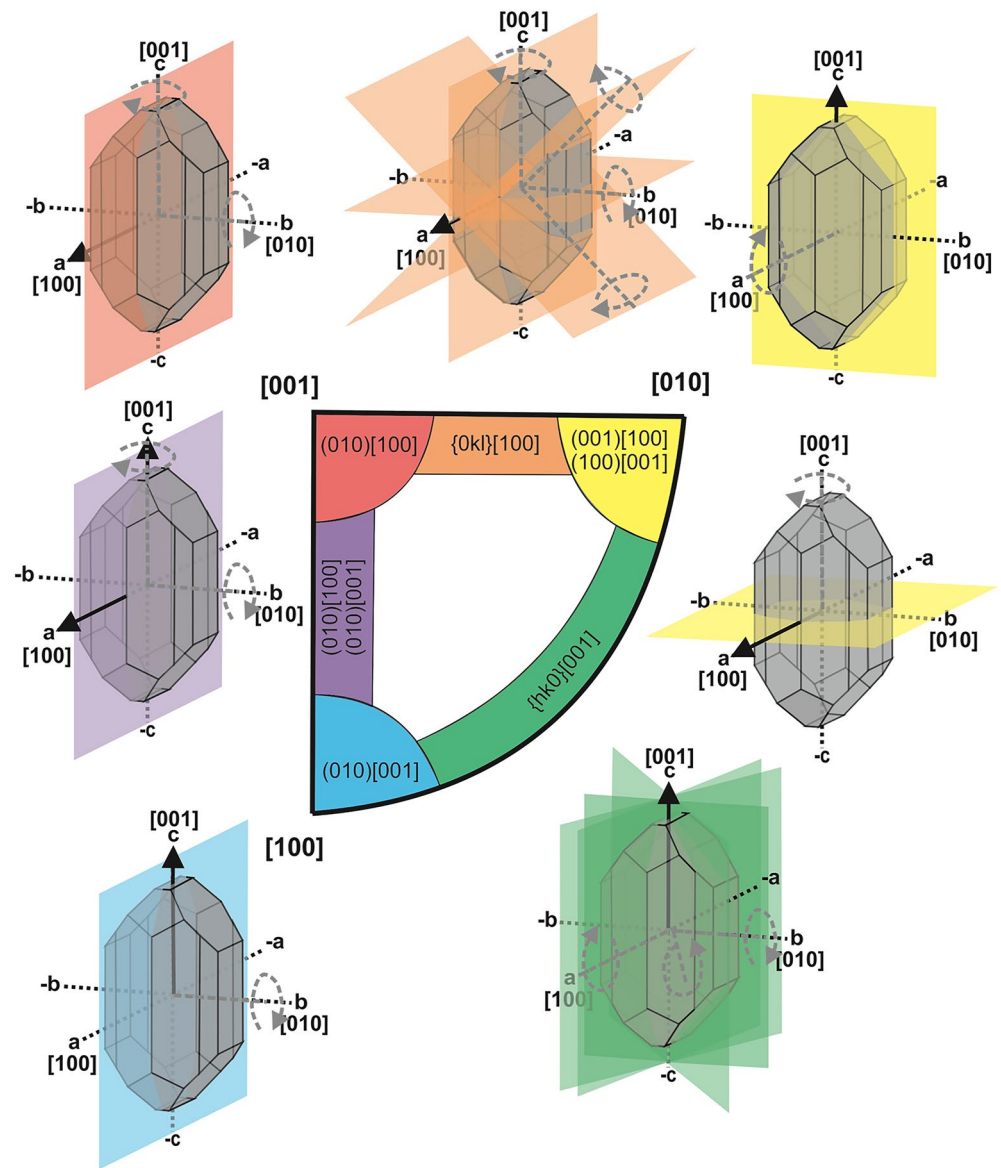


Figure 1. Olivine (forsterite; $mmm (2/m)$; unit cell lengths $a = 4.66$, $b = 10$, $c = 5.87$ angstrom) crystallographic slip-system signature key (notated as the slip plane and slip direction) expressed as the orthorhombic crystallographic fundamental sector (lowest form of crystal symmetry; modified from De Kloe et al. (2002); Ruzicka and Hugo (2018)). The corners of the key refer to olivine's specific crystallographic axis ($\langle a \rangle = [100]$, $\langle b \rangle = [010]$, and $\langle c \rangle = [001]$). The surrounding diagrams visualize the different slip planes where the straight black arrows indicate the direction of slip for both twist and tilt boundaries. For a tilt boundary [movement perpendicular (axis parallel) to the plane] the black arrows also indicate the tilt axis, whereas the plane rotation axis for a twist (*i.e.*, rotating) boundary [movement within (axis perpendicular) to the plane] is indicated by the gray dashed arrows.

The majority of Martian meteorites are mafic-ultramafic igneous rocks (Udry et al., 2020 and references therein). To date the Martian meteorites, consist of the clinopyroxene rich shergottites and nakhlites, orthopyroxenite ALH 84001, the dunitic chassignites, and a nonigneous group of polymict breccias. The nakhlites, the focus of this study, are currently considered the largest group of Martian rocks sourced from a singular location on Mars, due to their consistent 10.7 ± 0.8 Ma ejection age and tight crystallisation ages (Cohen et al., 2017; Udry et al., 2020). Nearly all of the meteorites within the group contain evidence of aqueous alteration on Mars in the form of iddingsites (Bunch & Reid, 1975; Hallis & Taylor, 2011; Krämer Ruggiu et al., 2020; Lee et al., 2015; Noguchi et al., 2009; Treiman, 2005; Udry et al., 2020), and have been shown to sample several temporally distinct igneous

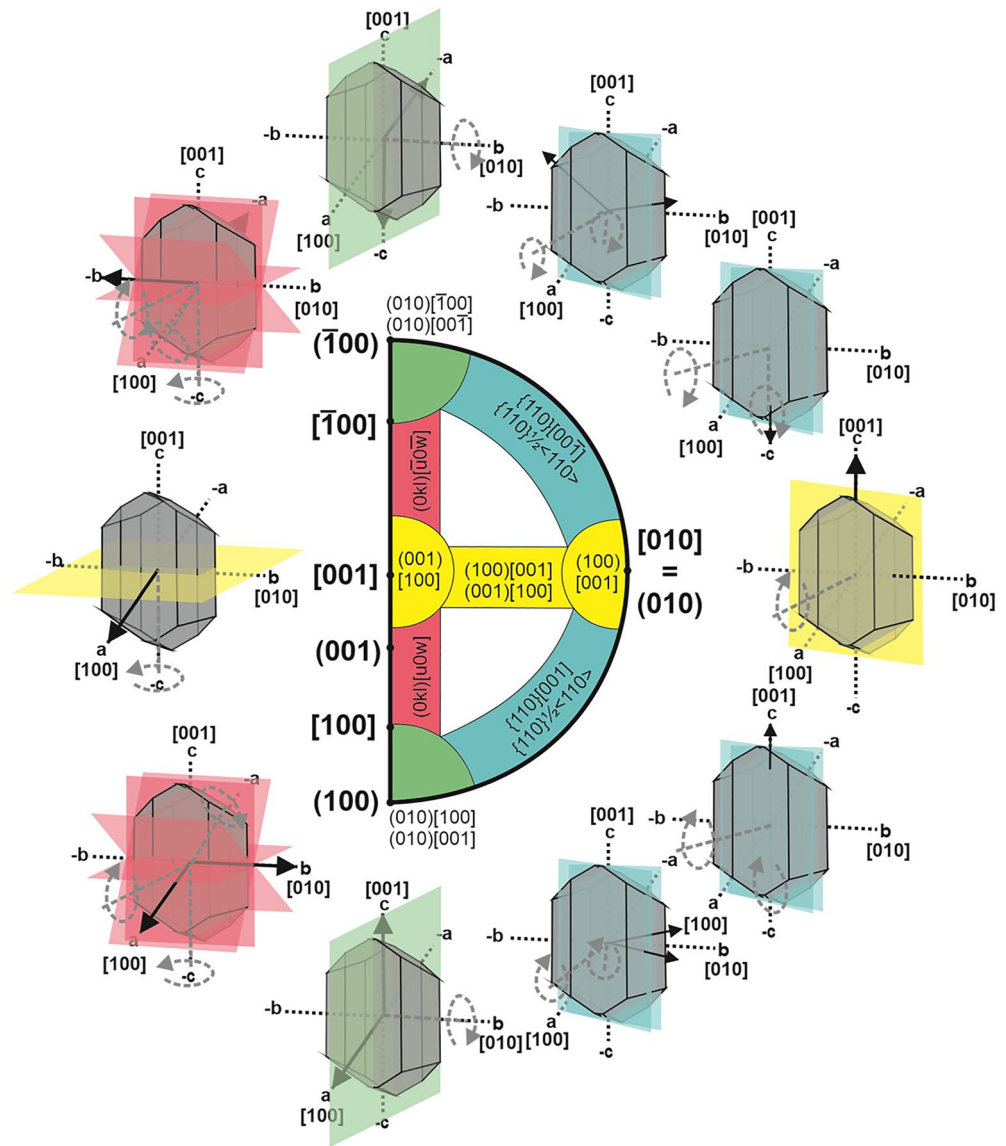


Figure 2. Augite (high Ca-clinopyroxene; 2/m (B2/b); unit cell lengths $a = 10.97$, $b = 10$, $c = 5.96$ angstrom) crystallographic slip-system signature key (notated as the slip plane and direction) expressed as the monoclinic crystallographic fundamental sector (lowest form of crystallographic symmetry). The outer bracketed labels of the key refer to augite's specific crystallographic axis ($\langle a \rangle = [100]$, $\langle b \rangle = [010]$, and $\langle c \rangle = [001]$). The surrounding diagrams visualize the different slip planes where the straight black arrows indicate the direction of slip for both twist and tilt boundaries. For a tilt boundary [movement perpendicular (axis parallel) to the plane] the black arrows also indicate the tilt axis whereas the plane rotation axis for a twist (*i.e.*, rotating) boundary [movement within (axis perpendicular) to the plane] is indicated by the gray dashed arrows.

events that are geochemically related by a shared magma source region (Cohen et al., 2017; Day et al., 2018; Treiman, 2005; Udry et al., 2020).

The nakhlites are basalts with crystal-sizes ranging from 0.29 to 1 mm, crystal clustering frameworks (Udry & Day, 2018), and low intensity low-moderate strength girdle CPO (Griffin et al., 2022). Their mafic composition is dominated by augite (55–71 modal%; Udry and Day (2018)) with low to moderate abundances of olivine (1.7–14.9 modal%). The remaining 0–42 modal% of the nakhlites is mesostasis consisting of varying proportions of clinopyroxene, orthopyroxene, olivine, plagioclase, titanomagnetite, iron sulphides, and glass (Corrigan et al., 2015; Udry & Day, 2018). Important for this study, the nakhlites contain low levels of shock (that is, high strain, maximum bulk shock pressures 5–20 GPa (Fritz, Artemieva, & Greshake, 2005)) that is variable

across the different specimens. Shock features within the group, reported to occur as bands within the samples, appear as reduced refractive index in plagioclase and deformation features (planar fractures, mechanical twinning, and undulose extinction) in olivine and pyroxene (Daly et al., 2019a, 2019b; Fritz, Artemieva, & Greshake, 2005). This deformational banding potentially indicates regions within the sample that could represent low strain (*i.e.*, mantle) deformation.

Majority of the work on augite and olivine deformation has been focused on understanding mantle (*i.e.*, low strain rate, low stress, high temperature) conditions. The nakhlites were ejected from the Martian surface by hypervelocity impact (Melosh, 1984). During impact ejection, the nakhlites were shock metamorphosed, which induces high strain rate deformation. This shock deformation although reported to be low in comparison to other Martian meteorites (Fritz, Artemieva, & Greshake, 2005), despite recent EBSD investigations suggesting the nakhlites were exposed to two impact events (Daly et al., 2019a). These hypervelocity impact events will have influenced and may have overprinted the magmatic deformation signatures within the nakhlites. However, the deformational banding observed suggests that the nakhlites could in fact exhibit deformation signatures related to both emplacement and ejection. This study asks the following: can crystallographic deformation parameters be used to further the understanding of rocky (planetary) bodies other than Earth, including the Moon, asteroids, and Mars? To tackle this question, olivine and clinopyroxene intracrystalline misorientation patterns formed from crystal plastic deformation (slip-systems) in the nakhlites are investigated.

2. Materials and Methods

Twenty-one EBSD data sets were collected for this study, covering sixteen individual nakhlite meteorites: Caleta el Cobre 022, Governador Valadares, Lafayette, Miller range (MIL) 03346, MIL 090030, MIL 090032, MIL 090136, Nakhla, Northwest Africa (NWA) 817, NWA 998, NWA 10153, NWA 11013, NWA 12542, Yamato (Y) 000593, Y 000749, and Y 000802 (Table 1). The presented EBSD data includes all known “paired stones” for the Miller Range (MIL) and Yamato (Y) nakhlites. Two sections of five meteorites: Governador Valadares, Nakhla, Northwest Africa (NWA) 998, Y 000593, and Y 000749 were also analyzed to assess the influence of experimental parameters as well as result consistency across different sections.

Prior to EBSD analysis each thick section was coated with a ~10 nm thick conductive carbon coat using a sputter coater. Prior to coating each section underwent both mechanical (iterative 1 μm followed by 0.3 μm aluminum spheres suspended in glycol for 5 min each), and chemical (4 hr using 0.1 μm colloidal silica suspended in a NaOH solution) polishing.

EBSD analyses were run using four different instruments in four different labs: ISAAC imaging center, University of Glasgow (Zeiss Sigma Field Emission Gun Variable Pressure Scanning Electron Microscope (FEG-VP-SEM) with Oxford Instruments NordlysMax² EBSD detector, operating Oxford Instruments AZtec analysis software v3.3); Geochemical Analysis Unit (GAU), Macquarie University (Carl Zeiss IVO SEM using a HKL NordlysNano high Sensitivity EBSD detector); Oxford Instruments Nanoanalysis HQ, High Wycombe (Hitachi SU70 FEG-SEM equipped with a Symmetry CMOS detector and indexed using AZtec analysis software v3.4); and the John de Laeter Centre, Curtin University (Tescan MIRA3 VP-FE-SEM with the NordlysNano EBSD detector and AZtec EDS/EBSD acquisition system). All analyses were run at 20 keV, 4–8 nA beam current, at a 70° tilt, under high vacuum (~3.4 $\times 10^8$ Pa) apart from MIL 03346 (118) and Lafayette (USNM 1505–1), which were run at low vacuum (~49 Pa). Selected step sizes (ranging 0.4–15 μm) for each sample were chosen to maximize the area covered by the EBSD maps and ensure data collection over available timeframes whilst ensuring the MAD values, and indicators of index quality, were <1 (all phases ranging 0.48–0.82; Table 1).

All EBSD data sets were processed using Oxford Instruments HKL Channel 5 software. Crystallographic axes for the forsterite and augite phases were defined as $b = 10 > c = 5.87 > a = 4.66$ angstrom (forsterite) and $a = 10.97 > b = 10 > c = 5.96$ angstrom (augite). To remove erroneous data (*i.e.*, mis-indexed, and nonindexed data points) without generating significant artifacts within the data sets, the data was first noise reduced using a wildspike correction followed by a consecutive 8–6 point nearest neighbor zero solution reductions (Bestmann & Prior, 2003; Daly et al., 2019a; Forman et al., 2016, 2019; Watt et al., 2006). Crystal boundaries were defined as >10° internal crystallographic misorientation from the nearest-neighbor pixel. Mechanical twins were identified as 180° rotation around augite (100), (204), or (104) axes and 60° rotation around forsterite (011), (012), and (100) axes. Simple twin boundaries were also identified in augite as 180° rotation around augite (001).

Table 1
Nakhlite EBSD Analysis Settings

	Caleta el Cobre 022	Governador Valadares		Lafayette	MIL 03346	MIL 090030	MIL 090032	MIL 090136	Nakhla	
	CERGE	BM.1975, M16, P8469	BM.1975, M16, P19783	USNM 1505-5	118	50	108	62	WAM 12965	USNM 426-1
Area (mm ²)	112.83	15.48	21.03	73.56	106.4	79.64	14.69	43.17	13.3	209.57
Pixel Count	16430075	1719852	93456	1659474	6653595	8848637	1631700	3606066	59450	2E+07
Hit Rate (%)	100	55.53	90.98	1659474	59.1	100	69.62	28.66	75.29	50.05
Section analysed	Partial	Whole	Partial	Partial	Partial	Partial	Partial	Partial	Partial	Partial
Step size (µm)	3	3	15	4	4	3	3	3	15	3
Tilt (°)	70	70	70	70	70	70	70	70	70	70
Accelerating voltage (keV)	20	20	20	20	20	20	20	20	20	20
Aperture (µm)	120	120	120	120	120	120	120	120	120	120
Beam Exposure (ms/EBSP)	24	28	30–40	30–40	30–40	21	26	24	30–40	28
Beam Current (nA)	21	4.1	8	4.1	4.1	21	4.1	4.1	8	21
Total (all phases)										
MAD	0.74	0.6	0.48	0.59	0.59	0.76	0.61	0.68	0.78	0.82
Mean BS	42.32	62.35	92.01	62.87	59.1	34.01	64.8	75.01	93.82	33.96
Mean BC	58.11	81.53	119.04	78.31	72.65	61.32	68.88	55.39	118.87	53.94
Augite										
MAD	0.76	0.56	0.48	0.65	0.59	0.8	0.65	0.68	0.78	0.82
Mean BS	43.64	69.44	91.9	56.31	58.53	32.91	62.33	74.89	93.39	33.76
Mean BC	57.42	90.5	118.90	66.54	71.14	58.1	65.15	54.96	118.05	53.17
Forsterite										
MAD	0.67	0.47	0.43	0.52	0.65	0.73	0.58	0.74	0.76	0.83
Mean BS	44.88	87.37	111.57	68.64	54.61	33.9	62.89	84.76	0.12	34.4
Mean BC	65.21	122.53	142.80	88.4	64.31	58.56	64.84	74.02	0.49	53.4
Bin criteria	4 × 4	4 × 4	4 × 4	4 × 4	4 × 4	1 × 1	4 × 4	4 × 4	4 × 4	4 × 4
EDS collected	Yes	Yes	Yes	Yes	Yes	Yes	Yes	Yes	Yes	Yes
Additional EDS map	Yes	No	No	No	No	Yes	Yes	Yes	No	No
Collected	CU	UofG	MU	UofG	UofG	CU	UofG	UofG	MU	CU

Note. EBSP = electron backscatter patterns a.k.a. Kikuchi diffraction patterns. CU = Curtin University. MAD = Mean angular deviation. MU = Macquarie University. BS = Band slope. UofG = University of Glasgow. BC = Back contrast. OIN = Oxford Instruments Nano-analysis, High Wycombe. EDS = electron dispersive spectroscopy.

NWA 817	NWA 998		NWA 10153	NWA 11013	NWA 12542	Y 000593		Y 000749		Y 000802
N8-1	T1	UG-1	SH65 T-2, 2	UG-1	F83-1	106-A	127-A	64-A	72-A	36-A
7.6	9.86	36.14	37.01	37.01	113.65	36.09	23.78	64.56	48.92	35.86
47493378	1578314	1784876	12537585	5921530	12627810	4E+06	2E+06	5928192	5546892	1434422
42.37	56.4	55.57	59.15	46.36	76.81	66.71	69.04	48.88	31.68	73.16
Partial	Whole	Partial	Partial	Partial	Partial	Whole	Partial	Partial	Whole	Partial
0.4	2.5	4.5	3	2.5	3	3	3.5	3.5	3	5
70	70	70	70	70	70	70	70	70	70	70
15	20	20	20	20	20	20	20	20	20	20
120	120	120	120	120	120	120	120	120	120	120
	24	26	25	32	25	29	26	26	30	24
12	4.1	4.1	18	4.1	4.1	4.1	4.1	4.1	4.1	4.1
0.56	0.69	0.7	0.82	0.69	0.57	0.67	0.55	0.73	0.66	0.66
104.81	50.68	0.08	39.19	52.65	68.86	51.54	87.91	50.35	68.97	53.4
96.77	57.46	0.38	47.71	62.47	82.56	62.34	98.45	51.79	78.05	65.8
0.56	0.71	0.71	0.84	0.69	0.56	0.65	0.54	0.75	0.66	0.69
104.81	50.67	48.54	40.27	51.67	70.93	54.4	88.99	48.7	68.17	50.43
96.77	57.12	55.68	47.86	60.58	84.12	67.97	99.3	48.26	76.64	59.57
0.57	0.62	0.6	0.78	0.6	0.49	0.7	0.46	0.64	0.69	0.57
106.54	56.6	56.8	40.04	61.95	73.62	52.06	104.4	54.87	72.89	58.69
98.05	71.25	73.69	49.18	81.24	91.23	60.85	122.3	61.92	85.03	77.04
4 × 4	4 × 4	4 × 4	4 × 4	4 × 4	4 × 4	4 × 4	4 × 4	4 × 4	4 × 4	4 × 4
Yes	Yes	Yes	Yes	Yes	Yes	Yes	Yes	Yes	Yes	Yes
No	No	No	No	No	Yes	No	Yes	Yes	No	Yes
OIN	UofG	UofG	CU	UofG	UofG	UofG	UofG	UofG	UofG	UofG

Meteorites, such as the nakhlites presented here, lack any consistent external reference frames. EBSD is a reference-frame based technique; thus, assigning a pseudo-external reference frame enables consistent comparison in the analysis across all the data sets. EBSD map principal orientations were arbitrarily defined as Y = top–bottom map direction, X = left–right map, and Z = direction perpendicular to the map plane. Grain (*i.e.*, crystal) reference orientation distribution (GROD) angle maps and local misorientation maps were used to identify regions of high deformation and low deformation within each of the nakhlites. Once the identified regions were checked against inverse pole figure (IPF), Euler, and phase maps specific subsets were created. All intracrystalline misorientation diagrams for both crystal reference frame (mIPF) and sample reference frame (mCPO; see supplementary material) plots (high deformation [H], low deformation [L], and whole section [$H + L$] data sets) were checked for map stitching artefacts before plotting. All plots were contoured using a maximum multiple uniform density (MUD, representing the density of data points) of 5, with 3° clustering, and a half width of 15° . Presented are the 2 – 10° mIPF plots for additional plots see the supplementary material. Indicative slip-systems present within each data set were identified from the MUD distribution patterns within the mIPF plots.

3. Results

3.1. Nakhlite Modal Mineralogy

Augite is observed as the dominant phase of 29.2 vol% (Y 000749 (72-A)) to 66.0 vol.% (Nakhla (WAM 12965)) in all collected data sets with variable proportions of olivine of 0.3 vol.% (MIL 03346 and NWA 11013) to 14.9 vol.% (Y 000593 (127-A); Figure 3). The mineralogy is observed to be heterogeneously dispersed with pockets of increased mesostasis abundance of 10 vol.% (Y 000593 (127-A)) to 60 vol.% (Caleta el Cobre 022) relative to phenocrysts of 9 vol.% (NWA 817) to 62 vol.% (Y 000593 (127-A); Figure 3).

3.2. Identification of Nakhlite High and Low Deformation Regions

Assessment of combined augite and olivine major mIPF patterns for all twenty-one analyzed nakhlite sections reveal nine distinct groupings (Figure 4). These nine groups are the culmination of both high and low strain deformation within the samples. However, GROD angle maps of the sections show defined regions of high and low deformation (*e.g.*, Figure 5). GROD maps are used to assess bending (*i.e.*, plastic deformation) within a given crystal. Here, the average orientation of a crystal is chosen as a fixed reference point and the amount of deviation in orientation is depicted from blue (0 (*i.e.*, same orientation)) to red (10° deviation (*i.e.*, the determined cutoff for a grain boundary)). Thus, within the GROD angle map, blue crystals indicate no bending within the crystal (interpreted as low strain (L)) and regions of yellowish-green to red depict bent regions within the crystal (interpreted as high strain (H)). In Figure 5, and other analyzed sections (see supplementary materials), high strain regions are observed to form as bands. These bands are typically located in mesostasis-rich and glass-rich regions, where the associated phenocrysts often exhibit increased density of fractures, and irregular linear features that do not produce higher diffraction patterns, as well as mechanical twins (white bands).

Out of the 21 analyzed sections, both NWA 10153 and NWA 11013 exhibit significantly less areas of low deformation ($<2^\circ$ GROD angles). In these sections the distribution of the higher deformation regions is observed to be more ubiquitous throughout the map area. Section Y 000593 (127-A) on the other hand, shows minimal internal deformation relative to the other analyzed sections, including its replicate section Y 000593 (106-A). Majority of the analyzed crystals within the section exhibit GROD angles $<1^\circ$, where the highest GROD angle observed is observed at $<5^\circ$ and restricted to smaller fractured crystals.

Within the analyzed nakhlites, augite exhibits two types of twins: simple twins (gray lines depicting 180° rotation about the {001} axis in augite) and mechanical twins (white lines representing the rotation of 180° and 60° around the {100} axis in augite and olivine, respectively). The simple twins are observed throughout the various analyzed sections appearing in both low and high deformation regions (Figure 5). The mechanical twins, however, only appear in high deformation regions (Figure 5). The mechanical twins appear with noticeable chevron patterns within augite crystals with higher GROD angle values or crystals on the boundary of regions of increased angle misorientation, particularly within samples Caleta el Cobre 022 (Figure 5), Gobernador Valadares (BM.1975,M16,P8469), Lafayette, MIL 03346, MIL 090032, NWA 817, NWA 10153, NWA 11013, NWA 12542, and Y 000593 (106-A). The mechanical twins are observed to span either the width of the crystal or where simple twinning is also present (occurring along the {001} axis in augite) and the mechanical twins form from

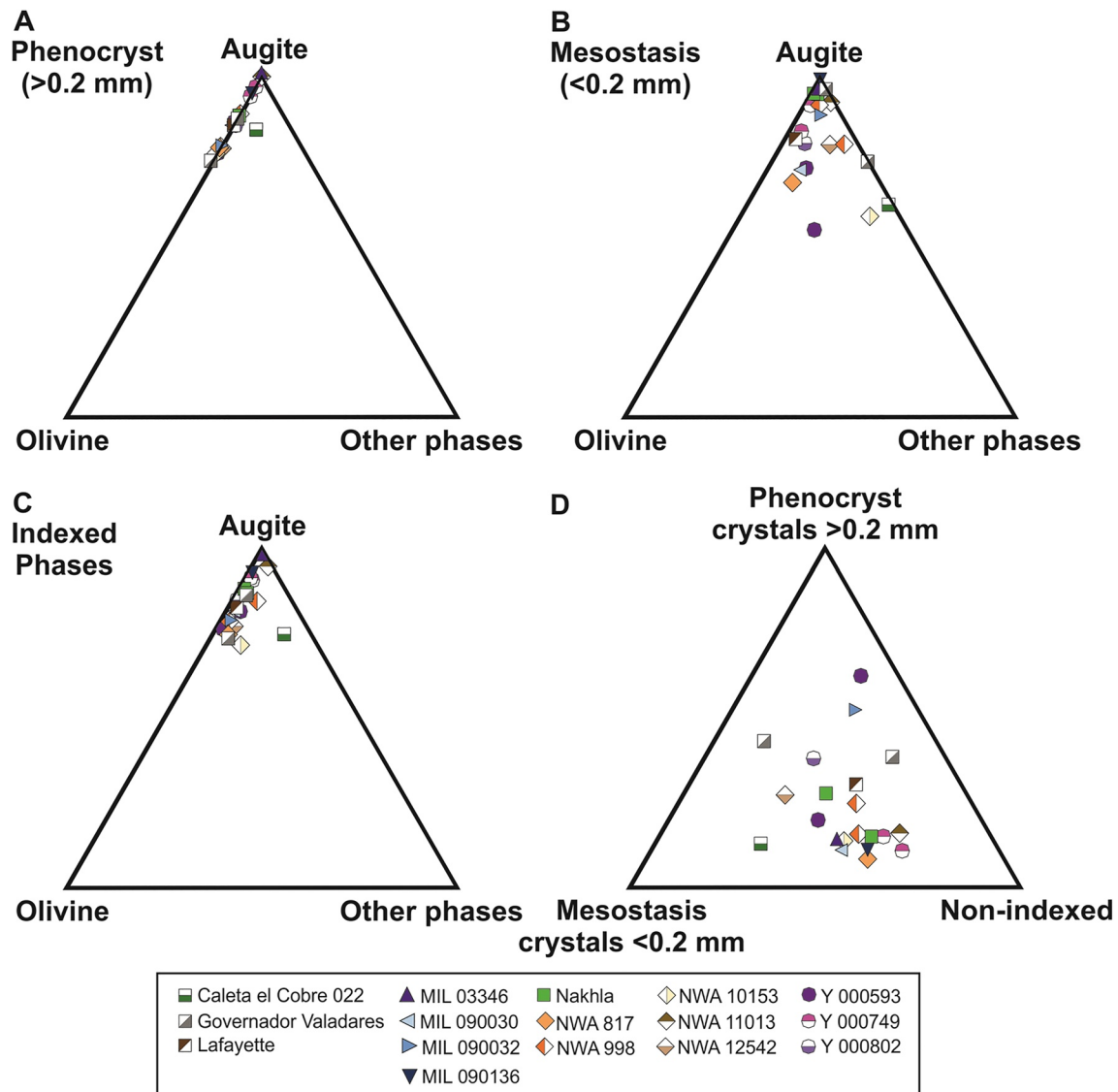


Figure 3. Compositional breakdown of EBSD data sets for analyzed nakhlite samples. (a) Compositional breakdown of indexed phenocrysts (>0.2 mm crystals). A higher proportion of other phases is observed within Caleta el Cobre 022 reflecting the increased abundance of plagioclase within the sample. (b) Compositional breakdown of indexed mesostasis (<0.2 mm crystals) (c) Compositional breakdown of all indexed phases (phenocrysts and mesostasis). (d) Distribution between phenocrysts crystals (>0.2 mm), mesostasis crystals (<0.2 mm), and nonindexed portions (representing the combination of voids/holes, glass, amorphous and other nonindexed phases) of the EBSD maps. For a full breakdown of indexed phases, please refer to the Table S1 and Figure S1 in Data Set S1.

the edge of the crystal into the simple twin boundary (light gray lines). Simple twins observed in augite appear throughout the sections appearing in both high and low deformation-designated regions (Figure 5).

Investigation of augite and olivine mIPF patterns for the depicted H and L regions within each analyzed section (e.g., Figure 5), reveal shifts in the observed patterns (Figures 6 and 7, Table 2). Overall, the dominant mIPF patterns identified in the H regions match those of the overall section mIPF patterns (Figures 4 and 6, Table 2) depicting nine different groups. However, changes in the pattern intensity and secondary mIPF patterns are observed (e.g., Figure 5). Within olivine (forsterite) mIPF plots (010)[001] combined with {hk0}(001) is observed as the most common mIPF pattern for nakhlite olivine (Group I (5 meteorites): Caleta el Cobre 022, Governador Valadares, Lafayette, NWA 12542, and Y 000593 (Figure 4)). Note that due to the low modal abundance of olivine within the overall samples (0.3–14.9 vol.%; Figure 3), the number of crystals contributing to the observed mIPF patterns are far below those recommended for statistically relevant and whole-rock representative results (5–84 crystals, i.e., <100 crystals; Watt et al., 2006) with the exception of NWA 12542 F83-I (136 crystals).

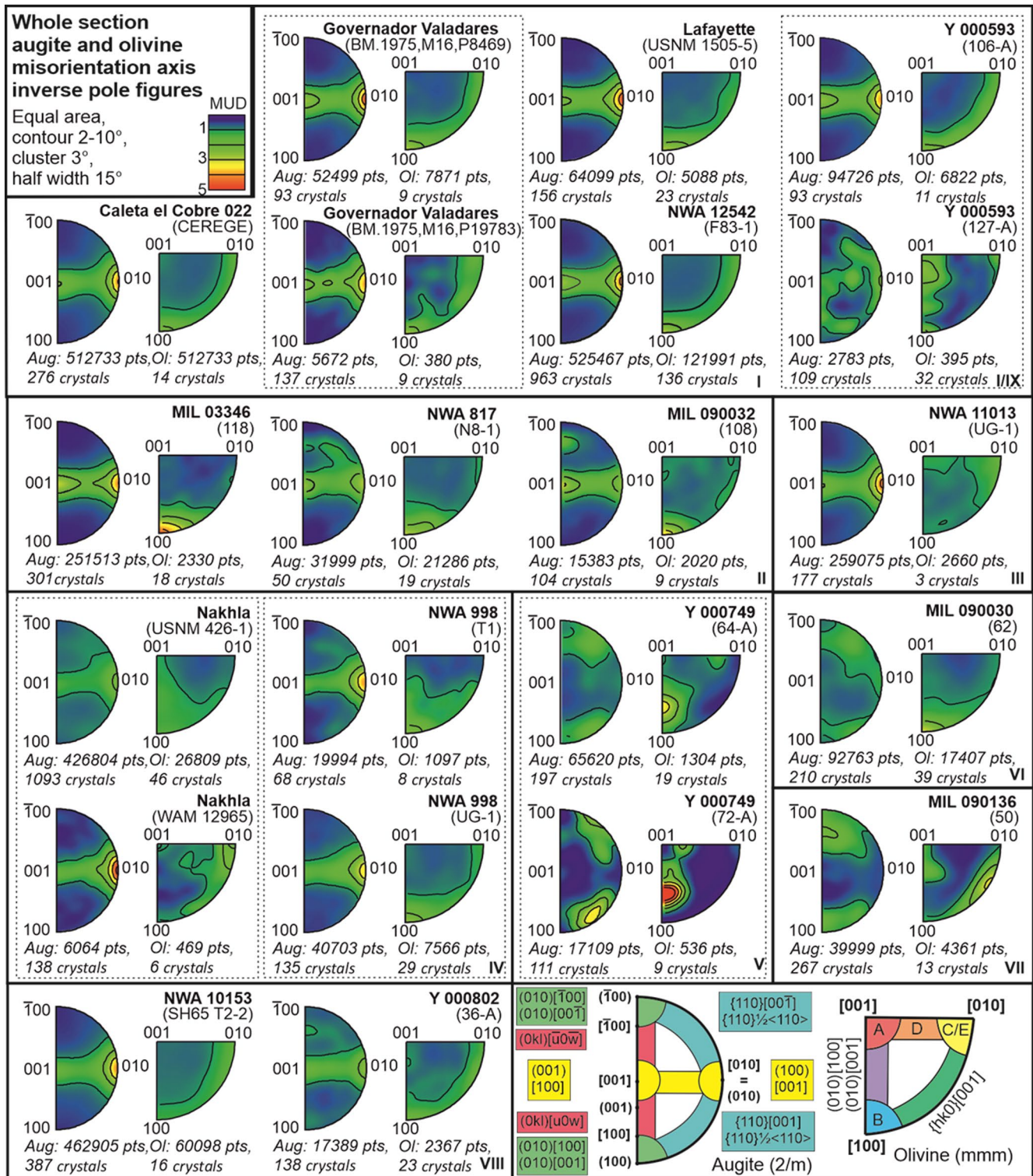


Figure 4. Intra-crystalline misorientation plots in crystal coordinate reference (mIPF) for naxhlite whole section data. Augite (half-circles) and olivine (quarter circles) represented as their fundamental sectors (lowest form of crystal symmetry). We identify 8 (potentially 9) different major mIPF pattern combinations for the naxhlites based on their respective keys (bottom right box) where each color indicates a different type of dominant slip-system. Olivine key: A = (010)[100], B = (010)[001], C = (100)[001], D = {0k1}[100], and E = (001)[100].

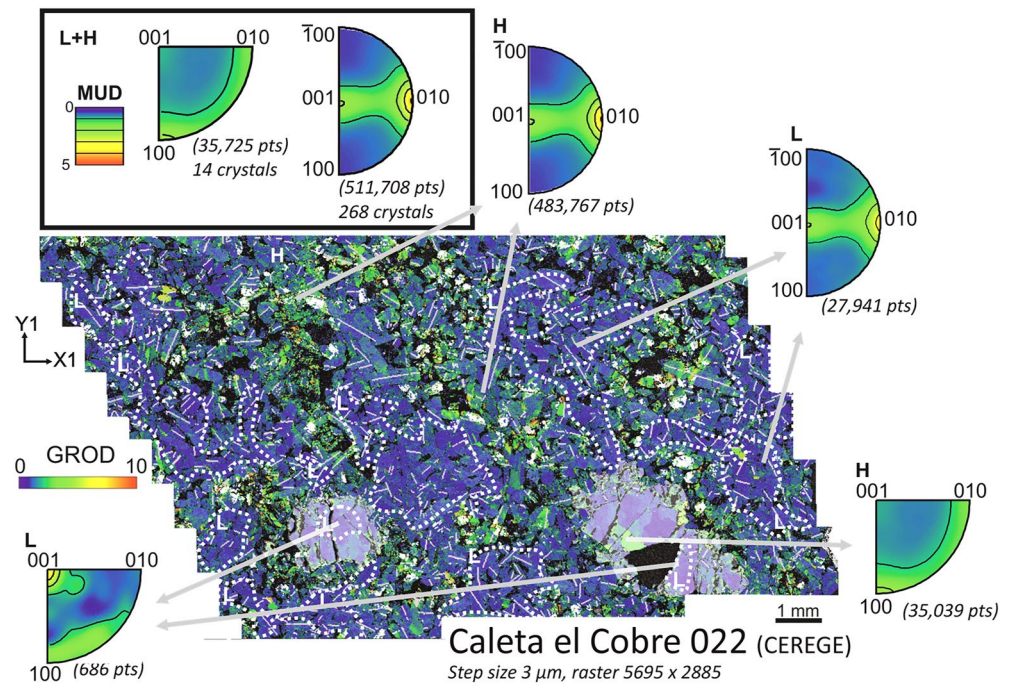


Figure 5. Grain relative orientation (GROD) angle map ($0\text{--}10^\circ$) Caleta el Cobre 022 (group I) with $2\text{--}10^\circ$ augite and olivine crystal reference intracrystalline misorientation patterns (mIPFs) for low deformation regions (L), high deformation regions (H), and the whole section representative mIPF patterns (L + H). The combined mIPF pattern is dominated by high deformation patterns. Between L and H mIPFs, a shift is observed in the olivine mIPF pattern while augite signatures remain constant. The GROD map depicts the changes in intracrystalline misorientation between 0 and 10° relative to the average intracrystalline misorientation. Bands of higher intracrystalline misorientation align with regions of increased mesostasis abundance. Augite and olivine mechanical twins [white lines; $\langle 100 \rangle$ axis in augite (180° rotation) and olivine (60° rotation)], and regions of higher fracture density. Augite simple twins (light gray lines, 180° rotation about $\langle 001 \rangle$ axis) an indicator of shock deformation appear throughout both the high and lower misorientation regions. Olivine within the sample is indicated by the white transparent layer. For additional maps, please refer to the supplementary materials Appendix 2.

Thus, the mIPF olivine plots presented below are included as a check for observed augite mIPF patterns but should not be considered representative on their own. Overall, five unique olivine mIPF patterns [$\{hk0\}$, $(010)[001]$, $(010)[100] + (010)[001]$, $(001)[100]/(100)[001]$, $(010)[001] + \{hk0\}$] are observed across the analyzed samples where the overriding mIPF pattern becomes clearly defined from the minor mIPF patterns with increased crystal count (Figure 6).

For augite, 4 out of the 21 EBSD data sets can be considered statistically relevant (>300 phenocryst crystals; Griffin, Daly, et al., 2022). 4 data sets contained <100 crystals (Governador Valadares (BM1975,M16,P8469), NWA 817 (N8-1), NWA 998 (T1), and Y 000593 (106-A); Figures 3–5). For augite four distinct mIPF patterns are identified with the two most commonly observed mIPF patterns involving the known pairing of $(100)[001]$ (major) and $(001)[100]$ (minor) dislocations expressed at varying proportions (groups I–III, VIII; Figure 6). Within Figure 6, groups I and II exhibit a higher proportion of $(001)[100]$ mIPF patterns compared to groups III and VIII (e.g., Figure 5). Augite $\{110\}[001] + \{110\}\frac{1}{2}\langle 110 \rangle$ mIPF patterns are also observed in groups V and VI, $(010)[100] + (010)[001]$ in group VII (MIL 090136), and a combination of multiple mIPF patterns, including components of $(100)[001]$, $(001)[100]$, $\{0kl\}\langle u0w \rangle$, $\{110\}[001] + \{110\}\frac{1}{2}\langle 110 \rangle$, within Y 000593 (Section 127-A; Figure 6).

When assessing the identified L regions dominant mIPF patterns were observed to shift but only for certain analyzed sections (that is, sections relating to nakhilites Caleta el Cobre 022 (Figure 5), NWA 817, NWA 11013, Nakhla, MIL 090030, MIL 090136, Y 000802, and Y 000593). Out of the nine identified high deformation region groups, excepting group V, at least one analyzed section exhibited different low deformation region mIPF patterns (Table 2, Figures 6 and 7). For the sections that showed different mIPF patterns between the H and L regions, pattern shifts were often only observed to occur in either olivine or augite, where olivine is the more likely

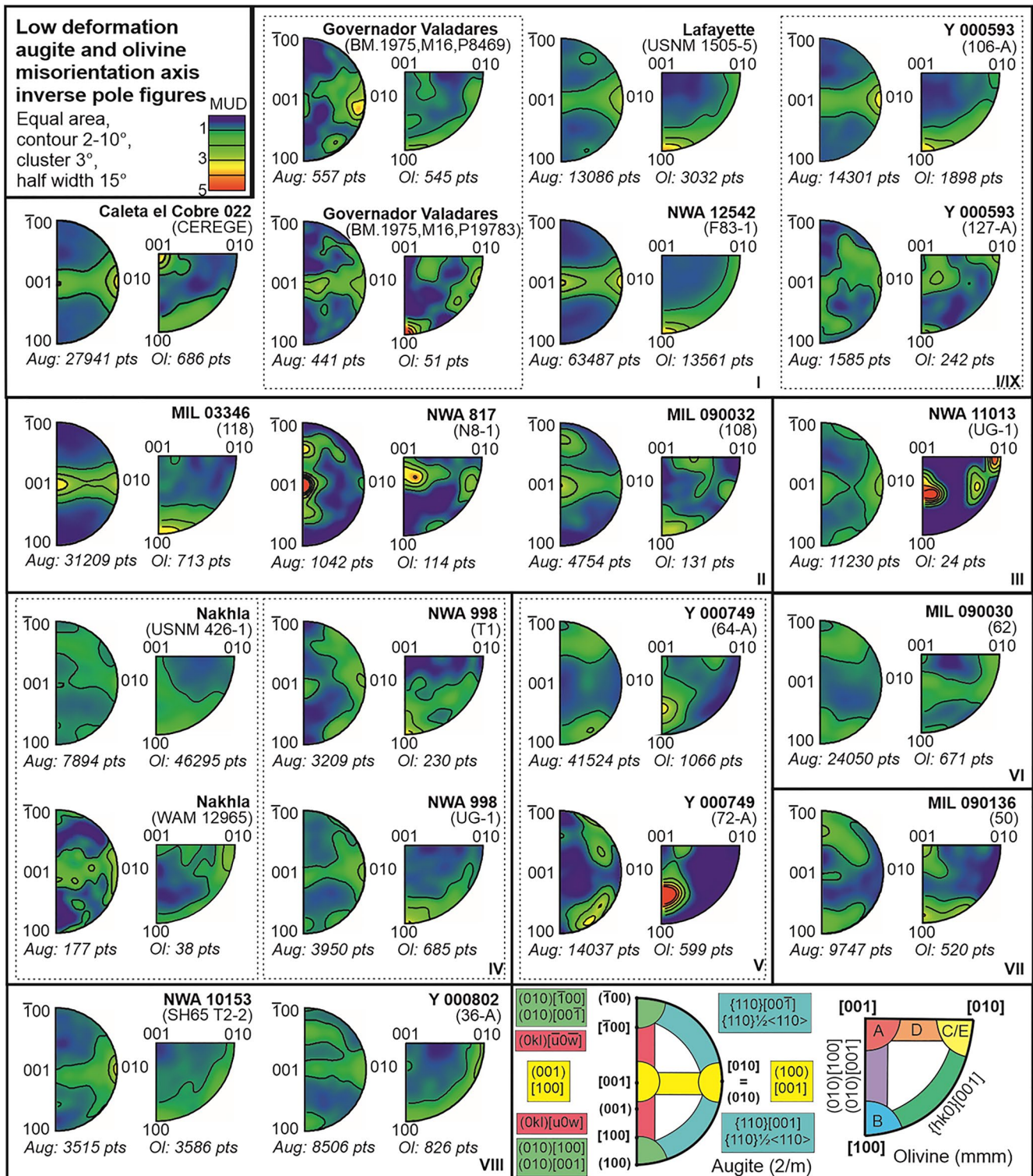


Figure 7. Low strain deformation mIPF plots for augite and olivine. Variation from high strain deformation mIPF patterns are observed for 9 of the 21 analyzed sections. Two different low strain mIPF patterns are observed within group II, while no significant shift in the mIPF pattern is observed for group V. mIPF patterns are based on the respective keys (bottom right box) where each color indicates a different type of the dominant slip-system. Olivine key: A = (010)[100], B = (010)[001], C = (100)[001], D = {0kl}[100], and E = (001)[100].

Table 2

Nakhlite Augite and Olivine Slip-System Patterns for High and Low Deformation Regions

	Nakhlite	section	high deformation region slip-system		Low deformation region slip-system*		
I	Caleta el Cobre 022*	CEREGE	Forsterite	I	Forsterite		
	Governador Valadares	BM1975,M16,P8469	(010)[001]+{hk0}[001]		(010)[100]+{hk0}[001]		
		BM1975, M16,P19783	Augite		Augite		
	Lafayette	USNM 1505-5	(100)[001]>(001)[100]		(100)[001]>(001)[100]		
	NWA 12542	F83-1					
Y 000593	106-A						
II	MIL 03346*	118	Forsterite	II	Forsterite*		
	MIL 090032	108	(010)[001]		(010)[001]		
	NWA 817* ¹	N8-1	Augite		Augite		
			(100)[001]+(001)[100]		(100)[001]<(001)[100]		
			Forsterite* ¹				
			II'	(010)[100]+{hk0}[001]			
				Augite			
				(001)[100]+(0kl)<u0w>			
III	NWA 11013*	UG-1	Forsterite	III	Forsterite		
			(100)[001]		(010)[u0w]+(100)[001]+(001)[100]		
			Augite		Augite		
			(100)[001]>>(001)[100]		(100)[001]>(001)[100]+{110}[001]+{110}1/2<110>		
IV	Nakhla*	USNM 426-1	Forsterite	IV	Forsterite		
		WAM 12965	(010)[001]+{hk0}[001]		(010)[001]+{hk0}[001]		
		NWA 998	T1		Augite	Augite	
		UG-1	(100)[001]>>(001)[100]		{110}[001]+{110}1/2<110>+(100)[001]		
V	Y 000749	64-A	Forsterite	V			
		72-A	(010)[100]+(010)[001]				
			Augite				
			{110}[001]+{110}1/2<110>				
VI	MIL 090030*	62	Forsterite	VI	Forsterite		
			(010)[001]		(010)[u0w]+{hk0}[001]		
			Augite		Augite		
			{110}[001]+{110}1/2<110>		{110}[001]+{110}1/2<110>		
VII	MIL 090136*	50	Forsterite	VII	Forsterite		
			{hk0}[001]		(010)[001]+(010)[u0w]		
			Augite		Augite		
			{010}<100>+{010}<001>		{010}<100>+{010}<001>		
VIII	NWA 10153	SH65 T-2, 2	Forsterite	VIII	Forsterite		
			Y 000802*		36-A	(001)[100]	(100)[001]+{hk0}[001]
					Augite	Augite	
			(100)[001]>>(001)[100]		(100)[001]+(001)[100]+(0kl)<u0w>		
IX	Y 000593*	127-A	Forsterite	IX	Forsterite		
			(010)[001]+(001)[100]+(0kl)[u0w]		(010)[001]+(001)[100]+{0kl}[u0w]		
			Augite		Augite		
			(100)[001]+(0kl)[u0w]		(100)[001]+(0kl)[u0w]		

Note. * and *¹ Indicate Samples for Which Either Augite, Olivine or Both Augite and Olivine Slip-System Patterns Have Changed Between Regions. N.B. Whole section slip system data exhibits the same slip-system patterns as those reported for the high deformation regions above.

mineral to exhibit a shift, most likely as a result of low crystal numbers (Figure 5, Table 2). However, additional shifts in mIPF patterns and intensity can also be observed as additional mIPF patterns within the *L* regions even when the major mIPF pattern remains the same (Figure 7). All *L* region mIPF patterns appear unique to the individual meteorite. More importantly, different low deformation mIPF patterns are observed to occur within group II (Table 2, Figure 7), where meteorites MIL 03346 and NWA 817 exhibit the same H region mIPF patterns but distinct *L* region mIPF patterns (Figures 6 and 7, Table 2). This indicates that the cause of the H region mIPF patterns are likely independent of the *L* region mIPF patterns.

To assess consistency in the presented analysis, replicate sections were run for five of the sixteen analyzed nakhlites. In these replicate sections, the same major augite and olivine mIPF patterns (both H and *L* region) are expressed for the meteorites Governador Valadares, NWA 998, and Y 000749. However, discrepancies in olivine mIPF patterns are observed between the two Nakhla sections {USNM 426–1 exhibiting (010)[001] H region patterns and WAM 12965 exhibiting (001)[100]/(100)[001] H region patterns} as well as differences in both augite and olivine mIPF patterns between the two Y 000593 sections {106-A exhibiting dominant (100)[001] with minor (001)[100] pattern for augite and (010)[001] with {hk0}[001] for olivine and Section 127-A exhibiting multiple dislocation patterns in augite and (010)[100]+(010)[001] for olivine}. Furthermore, low amounts of intracrystalline misorientation are observed within the GROD angle map. 120° triple junctions (typical annealing micro-structures) are also observed within Y 000593 (127-A)'s clustered olivine, which were not identified within Y 000593 (106-A). The observed variability of mIPF patterns within Nakhla and Y 000593 meteorites have direct implications for methodological parameters for example, step size and number of assessed crystals, textural heterogeneity, *etc.* which will be further evaluated in the discussion.

4. Discussion

4.1. Electron Backscatter Diffraction Mapping (EBSD) Appropriate Step Size for Intracrystalline Misorientation Pattern Determination

Mapping large areas using EBSD is becoming a more common tool for observing CPO within samples. The ability to analyze whole thin/thick sections however, is still a time-consuming and data intensive process — and is not without associated error (*e.g.*, mis-indexing, improper-indexing, beam drift *etc.*) even with recent technological advancements (Winiarski et al., 2021). The ability to cover larger areas is often counteracted by using larger step sizes, where the limiting factor for step size is controlled by the size of the crystal (to ensure >10 pixels/EBSD measurements are acquired per crystallite to adequately define its orientations), sacrificing higher resolution ($\leq 4 \mu\text{m}$ step size) required for microstructural analysis (Ruggles & Fullwood, 2013). Whilst microstructurally focused EBSD studies that utilize a smaller step size $\leq 4 \mu\text{m}$ will often observe either multiple single crystals from specific regions of a section or a selection of small areas where the total crystal count is below statistically stable results (<100–150 crystals; Vollmer, 1990; Skemer et al., 2005). Within the nakhlite data sets, five sections with a step size >4 μm (ranging from 4.5 to 15 μm) were run (Table 1), where three of these sections had a replicate section which was run at a step size <4 μm (Table 1). Replicate sections for two samples were also run at higher spatial resolution (*i.e.*, step size <4 μm). Comparing these replicate sections run at different step sizes clearer dominant mIPF patterns are able to be discerned from $\leq 4 \mu\text{m}$ particularly with smaller area maps. However, data presented here suggests that confirmation of similar mIPF patterns across multiple sections could be achieved using larger step sizes >4 μm on the condition that at least one of the sections is run at $\leq 4 \mu\text{m}$.

4.1.1. Analytical Limitations and Essential Criteria for Intracrystalline Misorientation Pattern Determination in Mapped EBSD Data Sets

Comparing results between replicate data sets, little difference is observed in the GROD angle distribution patterns between each section. However, the lower resolution in some of the data sets makes it more difficult to accurately assess the variability in the GROD angle across a given crystal that is, larger GROD angles are observed where most of the crystal is at a single value. The lower resolution of specific data sets also makes it difficult to ascertain the presence and interaction between a given crystal and any mechanical twinning present (Figure 5). Comparing mIPF plots for the replicate sections, the number of crystals analyzed is observed to have a greater impact on the determination, refinement, and identification of the samples' dominant major mIPF

pattern over the specific step size of the analysis (Figures 4, 6, and 7), with the caveat that the chosen step size is appropriate for the identification of intracrystalline misorientations that is, $\leq 4 \mu\text{m}$. Note that this observation is only relevant when assessing the overriding major mIPF patterns expressed within a section. To investigate microstructural changes between different deformation regions, inspect secondary mIPF patterns, or investigate how subcrystal boundary interactions in combination with crystal orientation contribute to the overall observed deformation, step sizes $\leq 4 \mu\text{m}$ are required.

4.1.2. Can EBSD-Derived Intracrystalline Misorientations Be Whole-Rock Representative?

Analysis of the replicate sections revealed consistent augite and olivine mIPF patterns for whole section, high deformation and low deformation data sets within Governador Valadares, NWA 998, and Y 000749 (Figures 6 and 7, Table 2). However, the same correlation is not observed within the replicate Nakhla or Y 000593 sections (Figures 6 and 7, Table 2). For the two Nakhla replicate sections there is consistency in the mIPF patterns of augite for all three data sets (whole section high deformation, and low deformation) and a discrepancy in expression of mIPF patterns in olivine where the types of mIPF patterns expressed are consistent but the dominant expressed mIPF pattern is different for whole section and high deformation data sets. The difference in expressed olivine mIPF patterns could be a function of the crystal differential (40 crystals and 26,340 data points) between the two data sets, the modal distribution of crystals between the sections, the larger (15 μm) step size of section WAM 12965 compared to USNM 426-1 (3 μm ; Table 1), or the heterogeneous influence and distribution of shock between the two sections in relation to olivine's location. More consistent MUD patterns are observed for augite within section USNM 426-1 (MUD = 0.53–1.37) compared to section WAM 12965 (MUD = 0.35–2.48) despite only USNM 426-1 containing CPO statistically relevant crystal numbers. A similar fluctuation in MUD values is also observed between the two replicate Governador Valadares sections. In this instance, consistent mIPF patterns are observed for all three data sets. In this instance each of the EBSD data sets sample equivalent crystals of olivine (9 crystals each) and augite crystals (93 vs. 137 crystals; Figure 4, Table 2). The only difference being a similar analysis step size discrepancy between the two Governador Valadares replicate sections as Nakhla (Table 1). This difference indicates the importance of comparable sized data sets for meaningful comparison between replicate sections. For both NWA 998 replicate sections which have a 0.5 μm step size differential and Y 000749 replicate sections which have the same analysis step size no fluctuations are observed in the dominant augite and olivine mIPF patterns. Across the naxhlite data sets statistically relevant crystal sets at $< 4 \mu\text{m}$ step size were observed to have cleaner MUD distribution patterns and narrower MUD ranges (for example, Governador Valadares MUD = 0.35–4.55 versus 0.25–3.56 (augite mIPF) and MUD = 0.55–2.72 versus 0.35–2.68 (olivine mIPF) for sections BM.1975,M16,P8469 and BM.1975,M16,P19783, respectively; Figures 4, 6 and 7, Table 1). Where decreased crystal count and larger step sizes contribute to increased MUD distributions within the mIPF plots (for example, Nakhla MUD = 0.63–2.30 versus 0.27–5.26 (augite mIPF) and 0.53–1.37 versus 0.34–2.48 (olivine mIPF) for sections USNM 426-1 and WAM 12965, respectively; Figures 4, 6 and 7; Table 2). Suggesting that differences observed within Nakhla's replicate section olivine mIPF patterns is most likely to be the result of both analysis step size and analysis area.

Out of all the replicate sections, only Y 000593 exhibited completely different augite mIPF patterns; (100)[001]:(001)[100] for Section 106-A and multiple mIPF patterns for Sections 127-A. Olivine mIPF patterns are also noncongruent (010)[001] with {hk0}[001] for Section 106-A and [100]+(010)[001] Section 127-A. In a low strain mantle system these mIPF patterns would indicate low temperature moderate strain conditions for Section 106-A and high temperature low strain condition for Section 127-A (Figures 4, 6, and 7). Multiple slip-systems as suggested by the observed Y 000593 (127-A) augite mIPF patterns that have been associated with partial melting and recrystallization conditions (Figure 7; Ave Lallemand, 1978), which would be consistent with observed olivine annealing micro-structures [120° triple junctions in clustered olivine) and lower dispersed deformation (GROD angle values). For section Y000593 (106-A) clear banding of high deformation can be observed within the GROD angle map, where mIPF patterns even within the low deformation regions still express high deformation region signatures (Table 2). Deformation, particularly which associated with shock metamorphism, is known to be heterogeneous (Stöffler et al., 2018). Variability in temperature and pressure resulting from hypervelocity impacts can create pockets within a sample that may have experienced higher temperature and/or pressure conditions. Furthermore, recrystallization has been shown to overprint a given crystal's deformation history to its new recrystallized conditions (Muto et al., 2011; Wenk & Tomé, 1999; Yao et al., 2019). Annealing

on the other hand has been shown to significantly reduce, overprint, and sometimes completely override a given crystal's former deformation history to the current conditions acting on the sample during the annealing process (Farla et al., 2011; H.; Jung et al., 2006). Investigations of shock deformation within the Yamato nakhlites has shown some of the lowest bulk shock pressures (5–14 GPa for Y 000593) within the already low shocked nakhlites (Fritz, Artemieva, & Greshake, 2005). However, the presence of annealing within the sample could have contributed to the lower inferred shock pressure values. Thus, the differences in mIPF patterns observed between the two Y 000593 sections could therefore indicate either an extreme change in emplacement environment, which would have had to occur within the cm scale of the meteorite stone (Imae et al., 2005), shock banding within the meteorite, or could indicate that the two sections represent two distinct neighboring geological units present within the same meteorite stone.

4.1.3. EBSD-Derived Intra-Crystalline Misorientation for Extrinsic Parameter Determination

Studies on assessing intracrystalline misorientation at a statistically relevant scale are still in their infancy. This is predominantly due to the specific cost, time, and equipment constraints (*e.g.*, beam stability, indexing time, computer processing ability, post processing time *etc.*) required to run $\leq 4 \mu\text{m}$ step size EBSD experiments. Comparison between collected EBSD data sets show that to use crystallographic slip-systems inferred from intracrystalline misorientations to assess extrinsic parameters within a given sample, higher spatial resolution (step sizes $\leq 4 \mu\text{m}$) EBSD maps are required to ensure reasonable and rational results (Figures 4, 6, and 7). Rocks in general are not homogeneous, while rocks that have experienced shock metamorphism (which in the case of MIL 03346, Lafayette, and most likely the entire nakhlite suite occurred on at least two occasions; Daly et al., 2019a, 2019b) exhibit even higher levels of microstructural and mineralogical heterogeneity (*e.g.*, Figure 5), through increased fracturing, partial melting, and partial recrystallization (Stöffler et al., 2018). Experimental data has shown that a crystal's orientation relative to external deformation parameters is one of many important factors for the selection and activation of particular slip-systems (Bascou et al., 2002; Bernard et al., 2019; Kollé & Blacic, 1982; Müller et al., 2008). Therefore, a relationship between CPO formation and slip-system activation would be expected even if it is not direct (Bascou et al., 2002; Karato et al., 2008; Katayama et al., 2005; Müller et al., 2008; Nagaya et al., 2014). The presence of nonrandom CPO within a sample predating post emplacement deformation (*e.g.*, shock metamorphism) should therefore help contribute to the development of dominant slip-systems being activated within a given sample by increasing the number of crystals oriented in a similar geometry with respect to the external strain field (Müller et al., 2008; Satsukawa & Michibayashi, 2009). Rocks, such as the nakhlites and other types of meteorites, which lack majority of the geological context used for terrestrial crystallographic deformation studies, such as sample orientation, require larger data sets to begin to enable valid interpretations to be made from the data. We would even go so far as to insist that for samples such as meteorites slip-systems from multiple phases should be considered (where possible) to help counteract the lack of geological context and often the smaller amount of available samples for analysis before crystallographic slip-systems are used to infer extrinsic deformation parameters for a sample as opposed to singular crystals.

4.2. The Correlation Between Slip-System Signatures and Deformation Conditions Observed in the Nakhlites

In order to compare observed olivine and augite mIPF patterns (Figures 6 and 7, Table 2) to deformation parameters, existing olivine diagrams (Figure 8) have been modified and equivalent diagrams created for clinopyroxene (Figure 9) using data from the literature. Note that the current extrinsic parameters presented in Figures 8 and 9 are based on low strain (*i.e.*, mantle induced) observations and experiments of not naturally occurring specimens exposed to high strain rates such as the nakhlites. Studies assessing mantle olivine have shown that extrinsic parameters for slip-systems can be much lower in value for naturally occurring samples compared to laboratory studies (Bernard et al., 2019) and references therein. It is therefore possible that the exact extrinsic parameters (axis values) stated for mantle augite and olivine in Figures 8 and 9 will be subject to change and may not be directly comparable to the presented data. However, the positioning of each slip-system signature relative to one another will remain constant enabling the use of both Figures 8 and 9 in a more qualitative manner.

Comparison of slip-system signatures in laboratory studies for both clinopyroxene and olivine has shown that although there are preferred slip-systems activation at specific conditions for a given mineral (Avé Lallemant, 1978; Bystricky & Mackwell, 2001; Gueguen & Nicolas, 1980; Ingrin et al., 1991; Jaoul & Raterron, 1994;

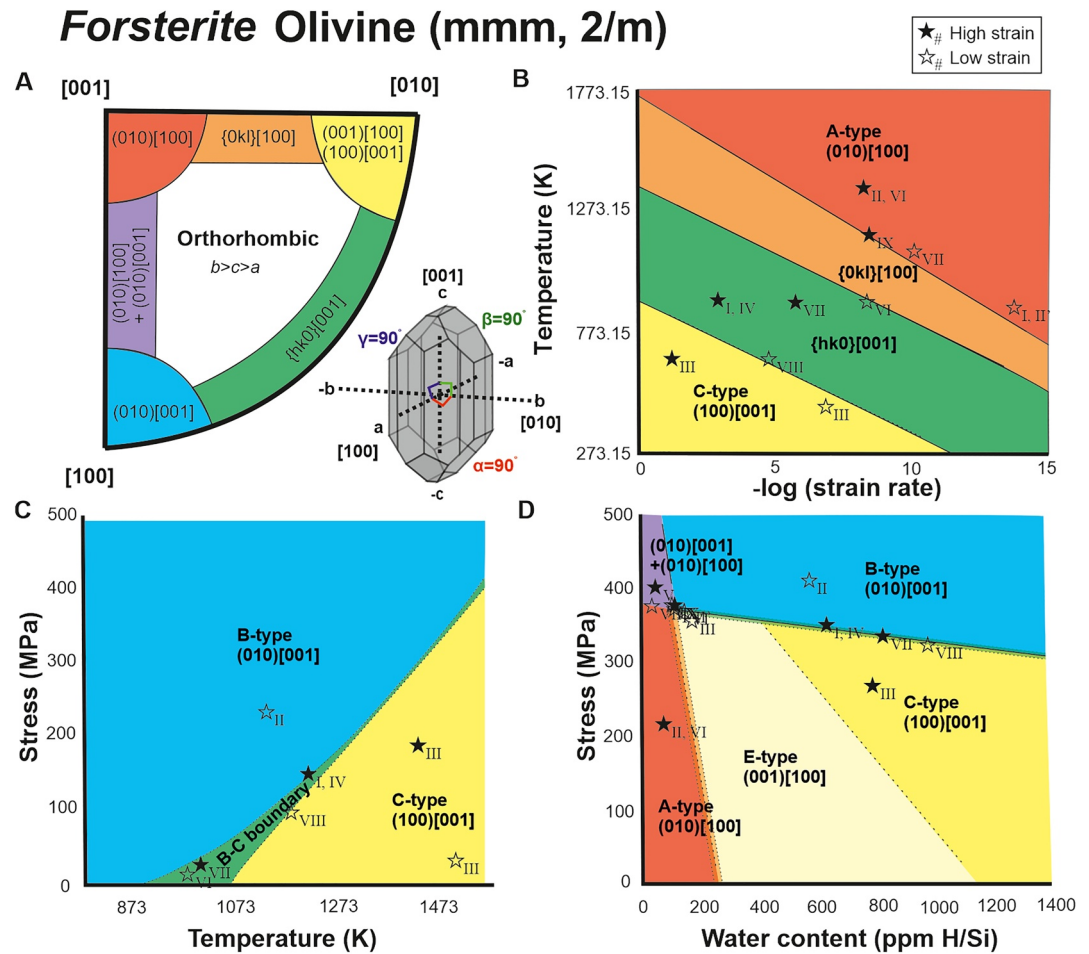


Figure 8. Known olivine (forsterite) slip-system deformation regions key (unit cells $b > c > a$). Colors indicate different slip-system regions. (a) Orthorhombic fundamental region slip-system key modified from (De Kloe et al., 2002; Ruzicka & Hugo, 2018) with a sketch of an olivine crystal illustrating its orthorhombic symmetry. (b) Temperature versus strain rate modified from (Katayama et al., 2004). (c) Stress versus Temperature modified from (Karato et al., 2008). (d) Stress versus water content modified from (Karato et al., 2008). Note. Extrinsic parameters are based off low strain data. Note. The placement of the identified nakhlite groupings (stars; Table 2) is only an indication of the related region and not absolute values.

Kollé & Blacic, 1982; Zhang et al., 2006), a given slip-system is not necessarily tied to any specific set of universal extrinsic parameters. These identified extrinsic parameters are also not specifically transferrable to different minerals, even those that share the same crystal symmetry due to the contribution of intrinsic parameters. Thus, even if naturally occurring sample data were available to construct Figure 9, there would still be overlap in slip-system regions between Figures 8 and 9, where CPO has been activated in one mineral and not another. These regions of slip-system overlap could potentially lend toward the use of multiple mineral slip-systems to better refine deformation parameters, if the extrinsic parameter values were properly quantified for the sample (unlike the nakhlites presented here). Note that for Figure 9 there is currently not enough existing data regarding the effect of water content on clinopyroxene slip-system signatures to realistically discuss this intrinsic parameter for the here presented nakhlite mIPF patterns. Thus, the presented results will only be discussed in terms of the external parameters: temperature and strain.

Variation between identified high and low deformation regions within the nakhlites identified from GROD angle maps suggests localization of deformation within the nakhlites (e.g., Figure 5). The identification and localization of mechanical twinning within identified high deformation regions suggest that the high deformation bands are related to shock deformation. This interpretation is in line with observed mIPF patterns (discussed below) and

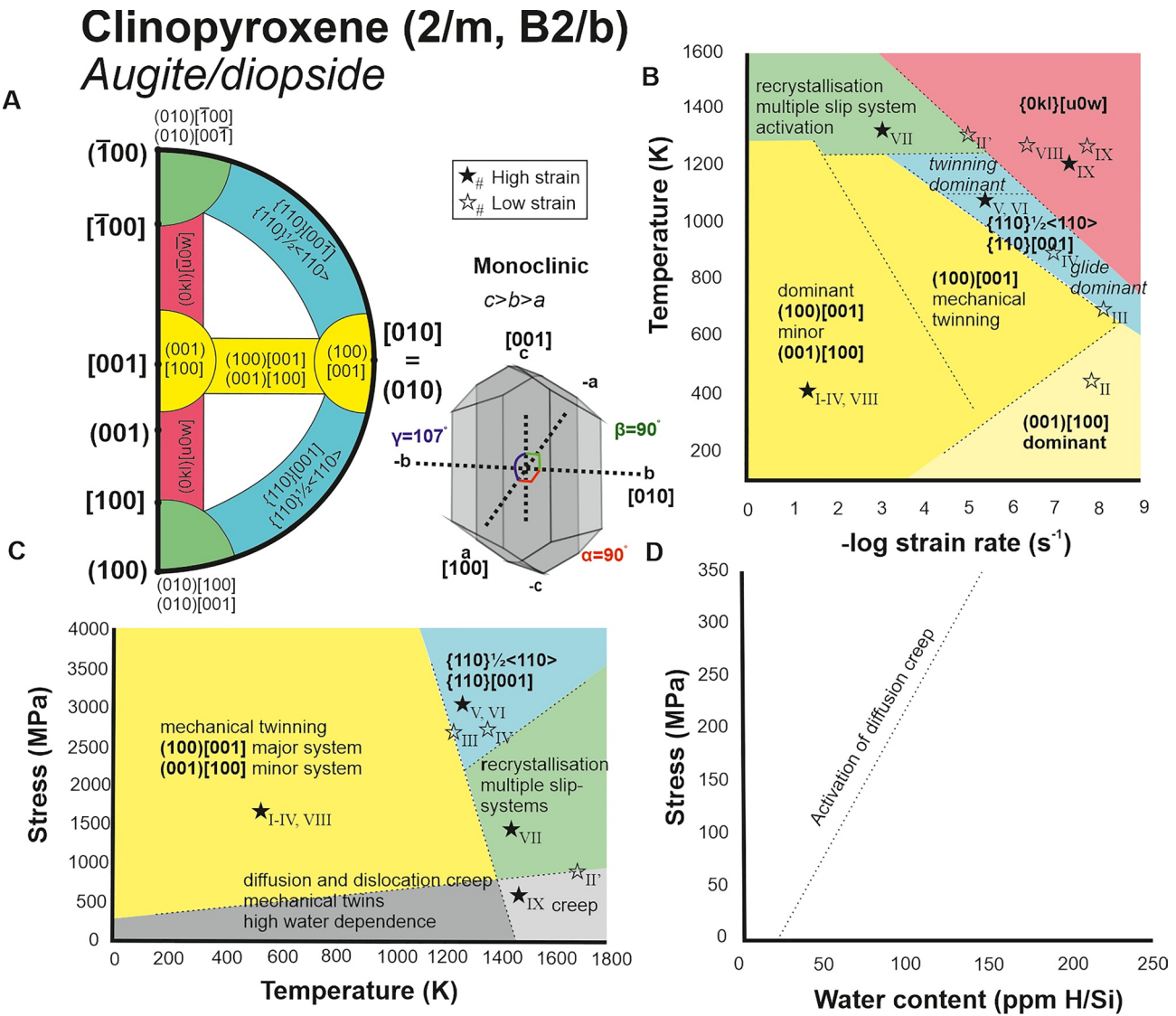


Figure 9. Proposed slip-systems deformation regions for the clinopyroxene (augite/diopside) key (unit cell $c > b > a$) based on published experimental data. Colors indicate different slip-system regions. (a) Monoclinic fundamental region slip-system key for unit cell $c > b > a$ with a sketch of an augite crystal illustrating its monoclinic symmetry. (b) Temperature versus strain rate (Avé Lallemant, 1978; Kollé & Blacic, 1982; Raleigh, 1967). (c) Stress versus Temperature (Avé Lallemant, 1978; Bystricky & Mackwell, 2001; Jaoul & Raterron, 1994; Kollé & Blacic, 1982; Müller et al., 2008; Zhang et al., 2006; Zhang & Green, 2007). (d) Stress versus water content (Hier-Majumder et al., 2005). Due to the paucity of experimental data involving augite deformation in the presence of water, currently we can only state that there is a trend of lower extrinsic parameters required to induce the activation of specific slip-system signatures in augite with increased water content. *Note.* a) Extrinsic parameters are derived from low strain data. *Note.* b) The placement of the identified nakhlite groupings (stars; Table 2) is only an indication of the related region and not absolute values.

previous analysis of the nakhlites where shock levels were calculated to range between 5 and 20 GPa (Fritz, Artemieva, & Greshake, 2005).

4.2.1. Impact Deformation Regime From mIPF Slip-System Patterns

Similarities between whole section and high deformation region compared to low deformation region mIPF patterns suggest that the localized high deformation regions are more prevalent in the nakhlites than the low deformation region deformation source. Out of the nine identified groups five expressed mIPF patterns more related to low temperatures and high strain, slip-systems while the other four (Groups V–VII, and IX) appear to be more dominated by higher temperature mIPF patterns Figures 6, 8, and 9).

Within the mineral olivine the direction of slip on the {010} lattice plane tends to respond the most significantly to temperature, whilst slip associated on either the {100} or {001} lattice plane appear to respond more readily to changes in strain (Figure 8). For the nakhlites, three of the six most commonly observed mIPF patterns are associated with strain. Comparison between whole section, high deformation, and low deformation region results show that the specific mIPF pattern relating to {hk0}[001] is observed to increase in intensity in the high deformation regions (Figures 4, 6, and 7; Table 2).

Augite within the nakhlites is observed to deform preferentially in the direction of <001> and <010> (Figure 2). These preferences result in the commonly observed (100)[001]:(001)[100] slip-system patterns (Figure 2) identified at most Earth relevant temperature, pressure, stress, and strain conditions (Figure 9). This preferential occurrence in (100)[001]:(001)[100] mIPF pattern matches observed crystallographic preferred orientation (CPO) patterns from naturally occurring samples, where high levels of compression for <010> and perpendicular alignment to the principal strain axis for <001> is observed (Frets et al., 2012; Mauler et al., 2000). Experimental studies have shown the amount of (001)[100] slip present in a given sample is observed to increase in response to greater amounts of strain at low temperatures (Figure 9). Between whole and high section mIPF patterns a slight increase in (001)[100] is observed within some of the samples (*e.g.*, Y 000802). Both groups I and II, encompassing eight of the 16 analyzed stones, exhibit mIPF patterns that relate increased proportions of (001)[100] within the (100)[001]:(001)[100] pairing (Figure 6). When comparing between the high deformation and low deformation regions, for all nakhlites exhibiting augite (100)[001]:(001)[100] mIPF patterns, the intensity of (001)[100] is observed to decrease in the low deformation mIPF plots (Figure 7; Table 2). This indicates an increase in low temperature high strain deformation being present within high deformation regions within the nakhlites.

Assessment of mIPF patterns suggest that impact deformation within the nakhlites is typically expressed as {hk0}[001] in olivine and increased proportions of (001)[100] within the (100)[001]:(001)[100] slip-system pairing in augite (Figures 6 and 7). However, it should be noted that the expression of impact-induced deformation is not solely restricted to the high GROD angle regions within a given nakhlite sample. Many of the observed low deformation region mIPF observed within the nakhlites still express remnants of the low temperature, high strain slip signatures (Figure 7, Table 2).

4.2.2. Emplacement, Low Finite Strain From mIPF Pattern Signatures

The occurrence of high deformation bands within the nakhlites in conjunction with their observed mIPF patterns indicates impact-derived deformation. This relation of high deformation bands to impact suggests the observed low deformation regions may provide evidence for emplacement. Out of the 16 analyzed nakhlites, only four stones showed evidence for high temperature deformation within the high deformation regions (Y 000749 (group V), MIL 090030 (group VI), MIL 090136 (Group VII), and Y 000593 (127-A; group IX)). The high temperature mIPF patterns observed in these regions were only seen to intensify in MUD values within the low deformation regions mIPF plots (Figures 6 and 7). Augite mIPF patterns in these groups are related to slip along the {110} lattice or along multiple crystallographic planes (Figures 2, 7, and 9). Olivine mIPF patterns indicate (010)[100] as the major slip signature (Figures 1, 6 and 8). It should be noted that the samples attributed to groups V–VII, and IX all exhibited low-detected GROD angles within the map areas. For identified groups I–IV, and VIII which all exhibit impact-related mIPF patterns had at least one analyzed section within the group that exhibited identifiable shifts in mIPF patterns between high and low deformation regions (Table 2). Assessment of the low deformation regions express mIPF patterns that emphasize patterns related to (010)[001] or (001)[100]/(100)[001] in olivine and (100)[001] in augite (Figure 7). (010)[100] slip is a common slip-system observed in mantle olivine's on Earth (Figure 8; (Bernard et al., 2019; Girard et al., 2013; Ohuchi et al., 2011; Yao et al., 2019). The presence of (100)[001] slip in augite is also commonly observed within nearly all naturally forming Earth samples (Bascou et al., 2002; Godard & van Roermund, 1995). Ultimately the mIPF patterns observed within these samples are typically associated with relatively low-moderate temperatures and low strain conditions (Figures 8 and 9) indicating that they are indeed remnants of emplacement deformation within the nakhlites that have been subsequently overprinted by impact-derived shock deformation.

4.2.3. Dominant Clinopyroxene Slip-Systems

From the two analyzed minerals augite shows the least diversity in mIPF slip-system patterns (Table 2). Laboratory experiments have shown that clinopyroxene slip-systems are strongly influenced by crystal orientation relative to the principal strain axis for the activation of specific slip-systems (Avé Lallemant, 1978; Bascou

et al., 2002; Kollé & Blacic, 1982). Clinopyroxenes, including augite, have one of the lowest forms of crystal symmetry (monoclinic, 2/m). The relationship between augite's crystallographic axes ($\alpha = 107^\circ$, $\beta = 90^\circ$, and $\gamma = 90^\circ$), where the crystallographic length of $\langle c \rangle > \langle a \rangle$, for augite's unit cell, will often require either specific orientation and/or higher strain for activation of slip-systems other than (100)[001]:(001)[100], such as {h0l} to form. Laboratory studies have also shown that even when such specific conditions are met to activate another of augite's slip-systems, (100)[001]:(001)[100] slip-systems will also often be observed within the sample (Avé Lallemant, 1978; Kollé & Blacic, 1983; Philippot & van Roermund, 1992).

For any geological sample, a variety of observed different slip-systems within a single sample would be expected. The expectation of variable slip-systems is in part due to the variation in alignment of crystals within a given rock and each crystal's local petrological context and surrounding mineral assemblage. For igneous samples, >50% crystal alignment is considered as strong SPO.CPO (Bunge, 1982; Vollmer, 1990). In the nakhlites, augite exhibits S- to LS-type CPO where crystal alignment ranges from 8% to 26% (Griffin et al., 2022). The higher percentage of random crystal orientations within any given sample coupled with a high dependence on crystal orientation for the activation of slip-system signatures will naturally result in multiple slip-system development between crystals. However, just like shape preferred orientation (SPO) and CPO within a rock, in order to assess representative deformation across a given sample several crystals preferentially on a similar level for statistical relevance (*i.e.*, ≥ 300 crystals for the nakhlites) would need to be assessed (Skemer et al., 2005; Vollmer, 1990). Overall, despite the low crystal symmetry and higher slip-system activation criteria in clinopyroxenes, differences between certain extrinsic conditions, for example, low temperature and high pressure, high temperature low pressure, and high temperature and pressure *etc.* can be observed (Figure 9). However, studies so far indicate for most Earth relevant conditions that the changes in slip-systems will be more subtle and be predominantly focused on shifts within the (100)[001]:(001)[100] slip-system pairing. Although clinopyroxene slip-systems have been identified to associate with specific conditions, there is a lot more work to be carried out. In particular, more information is needed addressing natural formation conditions and the effect of water content, before clinopyroxene slip-systems can be definitively used with the same level of certainty as geologists currently use olivine.

4.3. Implications for the Nakhlites' Time on Mars

Across the 16 analyzed nakhlite meteorites nine distinct mIPF pattern combinations for whole section data are observed (Figure 4) that reflect high strain deformation (Figure 6). These mIPF patterns, when separated into respective high and low deformation regions (Figs. 6 and 7, Table 2), indicate signatures that most likely reflect differences in shock deformation, agreeing with previously petrologically identified shock features (Fritz et al., 2005). Even low deformation regions within the analyzed nakhlites show a strong influence of high strain deformation (*e.g.*, shock) over low strain deformation signatures (*e.g.*, mantle). Hence the extrinsic parameters presented in Figures 8 and 9 will not be applicable to the nakhlites but the relationship between the different slip-systems can be applied. On this basis, the presented data show several different high-strain deformation environments from within the nakhlite source indicating heterogenous sampling (*i.e.*, spallation zone depth, and distance from impactite) of the ejection crater (Bowling et al., 2020).

Comparison between whole section, high deformation, and low deformation region mIPF patterns across the 21 analyzed sections show an increase in the mIPF patterns of {hk0}[001] in olivine and an increased (001)[100] component within the dominant augite (100)[001]:(001)[100] signature in high deformation regions. These particular slip-systems have been shown in mantle rocks to indicate increased strain at low temperatures (Figures 8 and 9; Cordier, 2002; Katayama et al., 2004; Kollé & Blacic, 1983; Mainprice et al., 2005; Mauler et al., 2000), which suggests that this particular olivine-augite IPF pattern combination often expressed as the dominant or secondary mIPF pattern within the nakhlites, particularly groups I–IV and VIII (Figures 5 and 6, Table 2), could be indicative of shock-induced deformation. Our hypothesis can be tested through shock recovery experiments on olivine and pyroxene to assess the shock-induced activation of specific slip-systems.

The establishment of olivine slip-systems under low-strain extrinsic parameters are well constrained where the influences of the extrinsic parameters are an ongoing and active field of research (Bernard et al., 2019). The relationship of augite to extrinsic parameters, on the other hand, has not been as consistently studied; olivine but has gained serious momentum over the last decade (for example, Bascou et al. (2011), Tedonkenfack et al. (2021), and Van der Werf et al. (2017)). Presented in this study is the first attempt to collate existing clinopyroxene

slip-system data to begin thinking about clinopyroxene slip-systems in a similar manner to olivine with respect to extrinsic parameters. Through comparing observed clinopyroxene (in this instance augite) MIPF slip-system patterns against published experimental data and the more-established olivine slip-system extrinsic parameters to ascertain patterns and commonalities (due to the data pertaining to low strain parameters), rough implications with respect to the nakhlites can be drawn. All the identified groups apart from groups V–VII, and IX (Table 2) exhibit slip-system patterns that are highly influenced by high strain deformation (Figure 6, Table 2). Groups V–VII and IX express slip-system patterns commonly associated in mantle rocks with high temperature deformation, and the difference being group V exhibiting patterns indicative of higher strain and group IX indicating mIPF slip-system patterns potentially related to annealing processes (Figures 8 and 9).

Separation of the high and low deformation regions within the nakhlites show that interpretation of mantle-derived parameters is more complex than just assessing regions of low deformation within the samples. Despite the nakhlites being described as relatively low shock samples (5–20 GPa (Fritz, Artemieva, & Greshake, 2005; Fritz, Greshake, & Stöffler, 2005)), mIPF patterns even within the low deformation regions still exhibit weakened high deformation region signatures, here interpreted as shock deformation (Figure 7). This finding could support the hypothesis of the nakhlite ejecta crater being positioned on the extremity of an older crater (Daly et al., 2019a, 2019b). Out of all the analyzed samples only 9 of the 21 sections showed significant shifts in either olivine and/or augite major mIPF patterns between separated high and low deformation regions (Table 2, Figures 6 and 7). In these samples, an increase in the MUD is observed within less dominant mIPF patterns and a weakening of the MUD for olivine {hk0}[001] and augite (001)[100] is typically observed. The implications of these observations indicate that there is potential for the observed minor mIPF patterns, which increase in MUD intensity within the low deformation region mIPF plots and could indicate nakhlite mantle-related deformation. However, further investigation is required before any interpretations could be made.

The current groupings presented in Figures 4, 6, and 7, and Table 2 indicate samples that share similar extrinsic parameters related to high strain deformation. This could be interpreted as samples exposed to similar conditions within the ejecta crater during launch. These groupings do not indicate that the samples are sourced from the same magmatic body as is evidence by samples MIL 03346 and NWA 817 within identified group II that show different mIPF patterns within their low deformation region mIPF plots despite sharing the same whole section and high deformation mIPF patterns (Table 2, Figures 4, 6, and 7). The same observation can be applied to the proposed “paired” Yamato and Miller Range nakhlites where different mIPF patterns are observed for both whole section (Figure 4) and identified low and high deformation regions (Figures 6 and 7, Table 2).

For the Yamato nakhlites, here categorized into groups I, V, VIII, and IX (Table 2) mIPF patterns express temperature differences that could not be resolved if they were located in the same position within the nakhlite ejecta crater and formed from the same magma body on Mars (Figures 8 and 9). The Miller Range nakhlites samples such as MIL 03346 and MIL 090032 could be related based off observed mIPF patterns (Figures 6 and 7, Table 2). However, both MIL 090030 and MIL 090030 exhibit mIPF patterns whose related extrinsic parameters do not support pairing with any of the Miller Range nakhlites (Figures 4, 6, and 7, Table 2).

Apart from the two Y 000593 sections, discussed above, each of the different Miller Range and Yamato samples are sourced from separate stones that were found in a similar location in Antarctica (Treiman, 2005). These locations are known glacial fields that are fed from a large catchment area. The variation observed in mIPF patterns between these “paired” stones implies different deformation parameters for the separate meteorites, which could indicate either a range of deformation environments with each meteorite being sourced from a different section within the same igneous body or could suggest that each individual meteorite represents its own separate flow/intrusion. From rudimentary scaling analysis of nakhlite emplacement mechanisms, the Miller Range nakhlites were indicated to form as larger igneous bodies, while the Yamato nakhlites were suggested to form as smaller igneous bodies (Griffin et al., 2022). Model results of smaller igneous bodies in conjunction with the observed differences in crystallographic deformation, similar recovery position, and geochronological dating (Cohen et al., 2017), currently support the hypothesis that the Yamato nakhlite stones formed as individual igneous units that were located in close proximity to one another on Mars while the model indicated a larger igneous body; current geochronological age resolution in combination with presented crystallographic mIPF patterns would suggest that the Miller Range nakhlites could represent different regions (or lobes) from a single igneous event (Griffin et al., 2022). Overall, variation in mIPF patterns observed from presented data, suggests that the suite of

nakhlite meteorites heterogeneously sample different igneous units and regions from within their launch crater on Mars.

5. Conclusions

Observed mIPF patterns can be used to discern between samples exposed to varying extrinsic parameters. However, more work (both natural samples and laboratory based) needs to be undertaken to further constrain the slip-system signature extrinsic parameters underlying mIPF patterns, particularly regarding the effects of high strain and water content. In addition, EBSD mapping at high spatial resolution has the potential to become a powerful technique to constrain extrinsic parameters associated with deformation (*i.e.*, pressure, temperature, strain, water content) of Martian magmas and other meteorites when combined with analysis of naturally occurring samples and laboratory experiments regarding slip-system activations.

Combined olivine and clinopyroxene mIPF patterns identified nine different mIPF pattern combinations within the nakhrites five of which were associated with high strain deformation interpreted as shock deformation. This shock (high strain) deformation is observed as increased proportions of (001)[100] in augite and {hk0}[001] in olivine. Investigation of mIPF patterns between identified high and low deformation regions within the data indicates high strain deformation to be prevalent through the sample, including within the low deformation regions. Less dominant mIPF patterns identified to increase in MUD intensity within the low deformation mIPF patterns could have the potential to represent low strain (mantle related) deformation. However, further work investigating the contributions of shock metamorphism and the exact relationship between high strain slip-system extrinsic parameters is required.

Data Availability Statement

Constraints on the emplacement of Martian nakhlite igneous rocks and their source volcano from advanced micro-petrofabric analysis/Can the magmatic conditions of the Martian nakhrites be discerned via investigation of clinopyroxene and olivine crystallographic slip-systems? (Version MTEX 5.7.0, MATLAB 2021a) [Dataset]. Zenodo. <https://doi.org/10.5281/ZENODO.5545821> (Griffin, et al., 2021).

Acknowledgments

For providing the samples used in this study we thank the NHM London, Japanese Antarctic Meteorite Research Centre, Smithsonian, NASA Meteorite Working Group, Macovich Collection, the Museum of Western Australia, Centre Européen de Recherche et d'Enseignement de Géosciences de l'Environnement (CEREGE), and the Institute of Meteoritics University of New Mexico. We thank the contributions of our two anonymous reviewers and David Prior whose comments greatly enhanced our manuscript. This work forms a portion of S.G.'s PhD thesis and was funded by the Science and Technology Facilities Council through grants ST/N000846/1 and ST/H002960/1 to M.R.L.). All data are available at Griffin, et al. (2022).

References

- Ashby, M. F. (1970). The deformation of plastically non-homogeneous materials. *Philosophical Magazine*, 21(170), 399–424. <https://doi.org/10.1080/14786437008238426>
- Ashby, M. F. (1983). Mechanisms of deformation and fracture. *Advances in Applied Mechanics*, 23, 117–177. [https://doi.org/10.1016/s0065-2156\(08\)70243-6](https://doi.org/10.1016/s0065-2156(08)70243-6)
- Avé Lallemant, H. G. (1978). Experimental deformation of diopside and websterite. *Tectonophysics*, 48(1–2), 1–27. [https://doi.org/10.1016/0040-1951\(78\)90083-5](https://doi.org/10.1016/0040-1951(78)90083-5)
- Barber, D. J., Wenk, H. R., Hirth, G., & Kohlstedt, D. L. (2010). Chapter 95 dislocations in minerals. In *Dislocations in Solids* (Vol. 16). Elsevier. [https://doi.org/10.1016/S1572-4859\(09\)01604-0](https://doi.org/10.1016/S1572-4859(09)01604-0)
- Bascou, J., Doucet, L. S., Saumet, S., Ionov, D. A., Ashchepkov, I. V., & Golovin, A. V. (2011). Seismic velocities, anisotropy and deformation in Siberian cratonic mantle: EBSD data on xenoliths from the udachnaya kimberlite. *Earth and Planetary Science Letters*, 304(1–2), 71–84. <https://doi.org/10.1016/j.epsl.2011.01.016>
- Bascou, J., Tommasi, A., & Mainprice, D. (2002). Plastic deformation and development of clinopyroxene lattice preferred orientations in eclogites. *Journal of Structural Geology*, 24(8), 1357–1368. [https://doi.org/10.1016/s0191-8141\(01\)00137-7](https://doi.org/10.1016/s0191-8141(01)00137-7)
- Bernard, R. E., Behr, W. M., Becker, T. W., & Young, D. J. (2019). Relationships between olivine CPO and deformation parameters in naturally deformed rocks and implications for mantle seismic anisotropy. *Geochemistry, Geophysics, Geosystems*, 20(7), 3469–3494. <https://doi.org/10.1029/2019GC008289>
- Bestmann, M., & Prior, D. J. (2003). Intragranular dynamic recrystallization in naturally deformed calcite marble: Diffusion accommodated grain boundary sliding as a result of subgrain rotation recrystallization. *Journal of Structural Geology*, 25(10), 1597–1613. [https://doi.org/10.1016/S0191-8141\(03\)00006-3](https://doi.org/10.1016/S0191-8141(03)00006-3)
- Boneh, Y., & Skemer, P. (2014). The effect of deformation history on the evolution of olivine CPO. *Earth and Planetary Science Letters*, 406, 213–222. <https://doi.org/10.1016/j.epsl.2014.09.018>
- Bowling, T. J., Johnson, B. C., Wiggins, S. E., Walton, E. L., Melosh, H. J., & Sharp, T. G. (2020). Dwell time at high pressure of meteorites during impact ejection from Mars. *Icarus*, 343, 113689. <https://doi.org/10.1016/j.icarus.2020.113689>
- Bunch, T. E., & Reid, A. M. (1975). The Nakhrites. Part I: Petrography and mineral chemistry. *Meteoritics*, 10(4), 303–315. <https://doi.org/10.1111/j.1945-5100.1975.tb01187.x>
- Bunge, H.-J. (1982). *Texture analysis in materials science: Mathematical methods*. In H.-J. Bunge (Ed.), Cuvillier Verlag. (Paperback). <https://doi.org/10.7312/chi-18840-001>
- Bystricky, M., & Mackwell, S. (2001). Creep of dry clinopyroxene aggregates with deformation in the dislocation creep. *Journal of Geophysical Research*, 106(B7), 13443–13454. <https://doi.org/10.1029/2001jb000333>

- Cohen, B. E., Mark, D. F., Cassata, W. S., Lee, M. R., Tomkinson, T., Smith, C. L., et al. (2017). Taking the pulse of Mars via dating of a plume-fed volcano. *Nature Communications*, 8(1), 640. <https://doi.org/10.1038/s41467-017-00513-8>
- Cordier, P. (2002). Dislocations and slip systems of mantle minerals. *Reviews in Mineralogy and Geochemistry*, 51(1), 137–179. <https://doi.org/10.2138/gsrmg.51.1.137>
- Corrigan, C. M., Velbel, M. A., & Vicenzi, E. P. (2015). Modal abundances of pyroxene, olivine, and mesostasis in nakhlites: Heterogeneity, variation, and implications for nakhlite emplacement. *Meteoritics & Planetary Sciences*, 50(9), 1497–1511. <https://doi.org/10.1111/maps.12492>
- Daly, L., Lee, M. R., Piazzolo, S., Griffin, S., Bazargan, M., Campanale, F., et al. (2019a). Boom boom pow: Shock-facilitated aqueous alteration and evidence for two shock events in the martian nakhlite meteorites. *Science Advances*, 5(9), 1–11. eaaw5549. <https://doi.org/10.1126/sciadv.aaw5549>
- Daly, L., Piazzolo, S., Lee, M. R., Griffin, S., Chung, P., Campanale, F., et al. (2019b). Understanding the emplacement of Martian volcanic rocks using petrofabrics of the nakhlite meteorites. *Earth and Planetary Science Letters*, 520, 220–230. [10.1016/j.epsl.2019.05.050](https://doi.org/10.1016/j.epsl.2019.05.050)
- Day, J. M. D., Tait, K. T., Udry, A., Moynier, F., Liu, Y., & Neal, C. R. (2018). Martian magmatism from plume metasomatized mantle. *Nature Communications*, 9(1), 4799. <https://doi.org/10.1038/s41467-018-07191-0>
- De Kloe, R., Drury, M. R., & Farrer, J. K. (2002). Determination of activated slip systems in experimentally deformed olivine-orthopyroxene polycrystals using EBSD. *Microscopy and Microanalysis*, 8(SUPPL. 2), 680–681. <https://doi.org/10.1017/S1431927602106404>
- Farla, R. J. M., Kokkonen, H., Gerald, J. D. F., Barnhoorn, A., Faul, U. H., & Jackson, I. (2011). Dislocation recovery in fine-grained polycrystalline olivine. *Physics and Chemistry of Minerals*, 38(5), 363–377. <https://doi.org/10.1007/s00269-010-0410-3>
- Fei, H., Hegoda, C., Yamazaki, D., Wiedenbeck, M., Yurimoto, H., Shcheka, S., & Katsura, T. (2012). High silicon self-diffusion coefficient in dry forsterite. *Earth and Planetary Science Letters*, 345–348, 95–103. <https://doi.org/10.1016/j.epsl.2012.06.044>
- Fleck, N. A., Muller, G. M., Ashby, M. F., & Hutchinson, J. W. (1994). Strain gradient plasticity: Theory and experiment. *Acta Metallurgica et Materialia*, 42(2), 475–487. [https://doi.org/10.1016/0956-7151\(94\)90502-9](https://doi.org/10.1016/0956-7151(94)90502-9)
- Forman, L. V., Bland, P. A., Timms, N. E., Collins, G. S., Davison, T. M., Ciesla, F. J., et al. (2016). Hidden secrets of deformation: Impact-induced compaction within a CV chondrite. *Earth and Planetary Science Letters*, 452, 133–145. <https://doi.org/10.1016/j.epsl.2016.07.050>
- Forman, L. V., Timms, N. E., Bland, P. A., Daly, L., Benedix, G. K., & Trimby, P. W. (2019). A morphologic and crystallographic comparison of CV chondrite matrices. *Meteoritics & Planetary Sciences*, 265(11), 2633–2651. <https://doi.org/10.1111/maps.13380>
- Frets, E., Tommasi, A., Garrido, C. J., Padrón-Navarta, J. A., Amri, I., & Targuisti, K. (2012). Deformation processes and rheology of pyroxenites under lithospheric mantle conditions. *Journal of Structural Geology*, 39, 138–157. <https://doi.org/10.1016/j.jsg.2012.02.019>
- Friedrich, J. M., Ruzicka, A., Macke, R. J., Thostenson, J. O., Rudolph, R. A., Rivers, M. L., & Ebel, D. S. (2017). Relationships among physical properties as indicators of high temperature deformation or post-shock thermal annealing in ordinary chondrites. *Geochimica et Cosmochimica Acta*, 203, 157–174. <https://doi.org/10.1016/j.gca.2016.12.039>
- Fritz, J., Artemieva, N. A., & Greshake, A. (2005). Ejection of martian meteorites. *Meteoritics & Planetary Sciences*, 40(9–10), 1393–1411. <https://doi.org/10.1111/j.1945-5100.2005.tb00409.x>
- Fritz, J., Greshake, A., & Stöffler, D. (2005). Micro-Raman spectroscopy of plagioclase and maskelynite in Martian meteorites: Evidence of progressive shock metamorphism. *Antarctic Meteorite Research*, 18, 96–116. 2005ASMR....18...96F
- Girard, J., Chen, J., Raterron, P., & Holyoke, C. W. (2013). Hydrolytic weakening of olivine at mantle pressure: Evidence of [100](010) slip system softening from single-crystal deformation experiments. *Physics of the Earth and Planetary Interiors*, 216, 12–20. <https://doi.org/10.1016/j.pepi.2012.10.009>
- Godard, G., & van Roermund, H. L. M. (1995). Deformation-induced clinopyroxene fabrics from eclogites. *Journal of Structural Geology*, 17(10), 1425–1443. [https://doi.org/10.1016/0191-8141\(95\)00038-F](https://doi.org/10.1016/0191-8141(95)00038-F)
- Griffin, S., Daly, L., Keller, T., Piazzolo, S., Forman, L. V., Lee, M. R., et al. (2021). Constraints on the emplacement of Martian nakhlite igneous rocks and their source volcano from advanced micro-petrofabric analysis (Version MTEX 5.7.0, MATLAB 2021a) [Dataset]. Zenodo. <https://doi.org/10.5281/ZENODO.5545821>
- Griffin, S., Daly, L., Keller, T., Piazzolo, S., Forman, L. V., Lee, M. R., et al. (2022). Constraints on the emplacement of Martian nakhlite igneous rocks and their source volcano from advanced micro-petrofabric analysis. *Journal of Geophysical Research: Planets*. e2021JE007080. <https://doi.org/10.1029/2021JE007080>
- Groves, G. W., & Kelly, A. (1963). Independent slip systems in crystals. *Philosophical Magazine*, 8(89), 877–887. <https://doi.org/10.1080/14786436308213843>
- Gueguen, Y., & Nicolas, A. (1980). Deformation of mantle rocks. *Annual Review of Earth and Planetary Sciences*, 8(1), 119–144. <https://doi.org/10.1146/annurev.ea.08.050180.001003>
- Hallis, L. J., & Taylor, G. J. (2011). Comparisons of the four Miller Range nakhlites, MIL 03346, 090030, 090032 and 090136: Textural and compositional observations of primary and secondary mineral assemblages. *Meteoritics & Planetary Sciences*, 46(12), 1787–1803. <https://doi.org/10.1111/j.1945-5100.2011.01293.x>
- Hansen, L. N., Zhao, Y. H., Zimmerman, M. E., & Kohlstedt, D. L. (2014). Protracted fabric evolution in olivine: Implications for the relationship among strain, crystallographic fabric, and seismic anisotropy. *Earth and Planetary Science Letters*, 387, 157–168. <https://doi.org/10.1016/j.epsl.2013.11.009>
- Henry, H., Tilhac, R., Griffin, W. L., O'Reilly, S. Y., Satsukawa, T., Kaczmarek, M.-A., et al. (2017). Deformation of mantle pyroxenites provides clues to geodynamic processes in subduction zones: Case study of the Cabo Ortegal Complex, Spain. *Earth and Planetary Science Letters*, 472, 174–185. <https://doi.org/10.1016/j.epsl.2017.05.028>
- Hier-Majumder, S., Mei, S., & Kohlstedt, D. L. (2005). Water weakening of clinopyroxene in diffusion creep. *Journal of Geophysical Research*, 110(7), 1–12. <https://doi.org/10.1029/2004JB003414>
- Hunter, R. H. (1996). Texture development in cumulate rocks. *Developments in Petrology*, 15(C), 77–101. [https://doi.org/10.1016/S0167-2894\(96\)80005-4](https://doi.org/10.1016/S0167-2894(96)80005-4)
- Imae, N., Ikeda, Y., & Kojima, H. (2005). Petrology of the Yamato nakhlites. *Meteoritics & Planetary Sciences*, 40(11), 1581–1598. <https://doi.org/10.1111/j.1945-5100.2005.tb00133.x>
- Ingrin, J., Doukhan, N., & Doukhan, J. C. (1991). High-temperature deformation of diopside single-crystal 2. Transmission electron-microscopy investigation of the defect microstructures. *Journal Of Geophysical Research-Solid Earth And Planets*, 96(B9), 14287–14297. <https://doi.org/10.1029/91JB01233>
- Jaoul, O., & Raterron, P. (1994). High-temperature deformation of diopside crystal 3. Influences of pO₂ and SiO₂ precipitation. *Journal of Geophysical Research*, 99(B5), 9423–9439. <https://doi.org/10.1029/93JB03363>
- Jung, H., Katayama, I., Jiang, Z., Hiraga, T., & Karato, S.-I. (2006). Effect of water and stress on the lattice-preferred orientation of olivine. *Tectonophysics*, 421(1–2), 1–22. <https://doi.org/10.1016/j.tecto.2006.02.011>

- Jung, H., Mo, W., & Green, H. W. (2009). Upper mantle seismic anisotropy resulting from pressure-induced slip transition in olivine. *Nature Geoscience*, 2(1), 73–77. <https://doi.org/10.1038/ngeo389>
- Kaboli, S., Burnley, P. C., Xia, G., & Green, H. W. (2017). Pressure dependence of creep in forsterite olivine: Comparison of measurements from the D-DIA and Griggs apparatus. *Geophysical Research Letters*, 44(21), 10939–10947. <https://doi.org/10.1002/2017GL075177>
- Karato, S., Jung, H., Katayama, I., & Skemer, P. (2008). Geodynamic significance of seismic anisotropy of the upper mantle: New insights from laboratory studies. *Annual Review of Earth and Planetary Sciences*, 36(1), 59–95. <https://doi.org/10.1146/annurev.earth.36.031207.124120>
- Katayama, I., Jung, H., & Karato, S. I. (2004). New type of olivine fabric from deformation experiments at modest water content and low stress. *Geology*, 32(12), 1045–1048. <https://doi.org/10.1130/G20805.1>
- Katayama, I., Karato, S. I., & Brandon, M. (2005). Evidence of high water content in the deep upper mantle inferred from deformation microstructures. *Geology*, 33(7), 613–616. <https://doi.org/10.1130/G21332.1>
- Katayama, I., & Karato, S. I. (2006). Effect of temperature on the B- to C-type olivine fabric transition and implication for flow pattern in subduction zones. *Physics of the Earth and Planetary Interiors*, 157(1–2), 33–45. <https://doi.org/10.1016/j.pepi.2006.03.005>
- Keppeler, R. (2018). Crystallographic preferred orientations in eclogites – a review. *Journal of Structural Geology*, 115(April), 284–296. <https://doi.org/10.1016/j.jsg.2018.04.003>
- Kollé, J. J., & Blacic, J. D. (1982). Deformation of single-crystal clinopyroxenes: 1. Mechanical twinning in diopside and hedenbergite. *Journal of Geophysical Research*, 87(B5), 4019–4034. <https://doi.org/10.1029/jb087ib05p04019>
- Kollé, J. J., & Blacic, J. D. (1983). Deformation of single-crystal clinopyroxenes: 2. Dislocation-controlled flow processes in hedenbergite. *Journal of Geophysical Research*, 88(B3), 2381–2393. <https://doi.org/10.1029/JB088B03p02381>
- Krämer Ruggiu, L., Gattacceca, J., Bevuouard, B., Udry, A., Debaille, V., Rochette, P., et al. (2020). Caleta el Cobre 022 martian meteorite: Increasing nakhlite diversity. *Meteoritics & Planetary Sciences*, 25(7), 1–25. <https://doi.org/10.1111/maps.13534>
- Law, R. D. (1990). Crystallographic fabrics: A selective review of their applications to research in structural geology. *Deformation Mechanisms, Rheology and Tectonics. Geological Society Special Publication*, 54(54), 352–355. <https://doi.org/10.1144/GSL.SP.1990.054.01.30>
- Lee, M. R., Tomkinson, T., Hallis, L. J., & Mark, D. F. (2015). Formation of iddingsite veins in the martian crust by centripetal replacement of olivine: Evidence from the nakhlite meteorite Lafayette. *Geochimica et Cosmochimica Acta*, 154, 49–65. <https://doi.org/10.1016/j.gca.2015.01.022>
- Li, Z. Y., Wen, D. P., Wang, Y. F., & Liu, X. (2020). An investigation of dislocation in olivine phenocrysts from the Hawaiian basalts. *Journal of Earth Sciences*, 31(6), 1183–1189. <https://doi.org/10.1007/s12583-020-1338-2>
- Liu, S., Tommasi, A., Vauchez, A., & Mazzucchelli, M. (2019). Deformation, annealing, melt-rock interaction, and seismic properties of an old domain of the equatorial atlantic lithospheric mantle. *Tectonics*, 38(4), 1164–1188. <https://doi.org/10.1029/2018TC005373>
- Mainprice, D., Bachmann, F., Hielscher, R., & Schaeben, H. (2015). Descriptive tools for the analysis of texture projects with large datasets using MTEX: Strength, symmetry and components. *Geological Society - Special Publications*, 409(1), 251–271. <https://doi.org/10.1144/SP409.8>
- Mainprice, D., Tommasi, A., Couvy, H., Cordier, P., & Frost, D. J. (2005). Pressure sensitivity of olivine slip systems and seismic anisotropy of Earth's upper mantle. *Nature*, 433(7027), 731–733. <https://doi.org/10.1038/nature03266>
- Mauler, A., Bystricky, M., Kunze, K., & Mackwell, S. (2000). Microstructures and lattice preferred orientations in experimentally deformed clinopyroxene aggregates. *Journal of Structural Geology*, 22(11–12), 1633–1648. [https://doi.org/10.1016/S0191-8141\(00\)00073-0](https://doi.org/10.1016/S0191-8141(00)00073-0)
- Mei, S., & Kohlstedt, D. L. (2000). Influence of water on plastic deformation of olivine aggregates 2. Dislocation creep regime. *Journal of Geophysical Research*, 105(B9), 21471–21481. <https://doi.org/10.1029/2000jb900180>
- Melosh, H. J. (1984). Impact ejection, spallation and the origin of meteorites. *Icarus*, 59(2), 234–260. [https://doi.org/10.1016/0019-1035\(84\)90026-5](https://doi.org/10.1016/0019-1035(84)90026-5)
- Müller, W. F., Walte, N., & Miyajima, N. (2008). Experimental deformation of ordered natural omphacite: A study by transmission electron microscopy. *European Journal of Mineralogy*, 20(5), 835–844. <https://doi.org/10.1127/0935-1221/2008/0020-1851>
- Muto, J., Hirth, G., Heilbronner, R., & Tullis, J. (2011). Plastic anisotropy and fabric evolution in sheared and recrystallized quartz single crystals. *Journal of Geophysical Research*, 116(2), 1–18. <https://doi.org/10.1029/2010JB007891>
- Nagaya, T., Wallis, S. R., Kobayashi, H., Michibayashi, K., Mizukami, T., Seto, Y., et al. (2014). Dehydration breakdown of antigorite and the formation of B-type olivine CPO. *Earth and Planetary Science Letters*, 387, 67–76. <https://doi.org/10.1016/j.epsl.2013.11.025>
- Noguchi, T., Nakamura, T., Misawa, K., Imae, N., Aoki, T., & Toh, S. (2009). Laihunite and jarosite in the Yamato 00 nakhlites: Alteration products on Mars? *Journal of Geophysical Research*, 114(10), 1–13. <https://doi.org/10.1029/2009JE003364>
- Ohuchi, T., Kawazoe, T., Nishihara, Y., Nishiyama, N., & Irfune, T. (2011). High pressure and temperature fabric transitions in olivine and variations in upper mantle seismic anisotropy. *Earth and Planetary Science Letters*, 304(1–2), 55–63. <https://doi.org/10.1016/j.epsl.2011.01.015>
- Philippot, P., & van Roermund, H. L. M. (1992). Deformation processes in eclogitic rocks: Evidence for the rheological delamination of the oceanic crust in deeper levels of subduction zones. *Journal of Structural Geology*, 14(8/9), 1059–1077. [https://doi.org/10.1016/0191-8141\(92\)90036-V](https://doi.org/10.1016/0191-8141(92)90036-V)
- Poirier, J.-P. (1975). On the slip systems of olivine. *Journal of Geophysical Research*, 80(29), 4059–4061. <https://doi.org/10.1029/jb080i029p04059>
- Poirier, J.-P. (1982). On transformation plasticity. *Journal of Geophysical Research*, 87(B8), 6791–6797. <https://doi.org/10.1029/jb087ib08p06791>
- Poirier, J.-P. (1995). *Creep of crystals: High-temperature deformation processes in Metals, ceramics and minerals*. Cambridge University Press.
- Poirier, J.-P. (1995). Mineral physics and. In T. J. Ahrens (Ed.), *Mineral physics and crystallography: A handbook of physical constants* (pp. 245–252). American Geophysical Union. <https://doi.org/10.4324/9780203121146-35>
- Poirier, J.-P., & Nicolas, A. (1975). Deformation-induced recrystallization due to progressive misorientation of subgrains, with special reference to mantle peridotites. *The Journal of Geology*, 83(6), 707–720. <https://doi.org/10.1086/628163>
- Préçigout, J., & Hirth, G. (2014). B-type olivine fabric induced by grain boundary sliding. *Earth and Planetary Science Letters*, 395, 231–240. <https://doi.org/10.1016/j.epsl.2014.03.052>
- Qi, C., Hansen, L. N., Wallis, D., Holtzman, B. K., & Kohlstedt, D. L. (2018). Crystallographic preferred orientation of olivine in sheared partially molten rocks: The source of the “a-c Switch”. *Geochemistry, Geophysics, Geosystems*, 19(2), 316–336. <https://doi.org/10.1002/2017GC007309>
- Raleigh, C. B. (1967). Plastic deformation of upper mantle silicate minerals. *Geophysical Journal of the Royal Astronomical Society*, 14(1–4), 45–49. <https://doi.org/10.1111/j.1365-246X.1967.tb06220.x>
- Raterron, P., Chen, J., Geenen, T., & Girard, J. (2011). Pressure effect on forsterite dislocation slip systems: Implications for upper-mantle LPO and low viscosity zone. *Physics of the Earth and Planetary Interiors*, 188(1–2), 26–36. <https://doi.org/10.1016/j.pepi.2011.06.009>
- Raterron, P., Doukhan, N., Jaoul, O., & Doukhan, J. C. (1994). High temperature deformation of diopside IV: Predominance of [110] glide above 1000°C. *Physics of the Earth and Planetary Interiors*, 82(3–4), 209–222. [https://doi.org/10.1016/0031-9201\(94\)90073-6](https://doi.org/10.1016/0031-9201(94)90073-6)
- Raterron, P., & Jaoul, O. (1991). High-temperature deformation of diopside single crystal: 1. Mechanical data. *Journal of Geophysical Research*, 96(B9), 14277–14286. <https://doi.org/10.1029/91JB01205>
- Ruggles, T. J., & Fullwood, D. T. (2013). Estimations of bulk geometrically necessary dislocation density using high resolution EBSD. *Ultramicroscopy*, 133, 8–15. <https://doi.org/10.1016/j.ultramic.2013.04.011>

- Ruzicka, A. M., & Hugo, R. C. (2018). Electron backscatter diffraction (EBSD) study of seven heavily metamorphosed chondrites: Deformation systematics and variations in pre-shock temperature and post-shock annealing. *Geochimica et Cosmochimica Acta*, 234, 115–147. <https://doi.org/10.1016/j.gca.2018.05.014>
- Satsukawa, T., & Michibayashi, K. (2009). Determination of slip system in olivine based on crystallographic preferred orientation and subgrain-rotation axis: Examples from Ichinomegata peridotite xenoliths, Oga peninsula, akita prefecture. *The Journal of the Geological Society of Japan*, 115(6), 288–291. <https://doi.org/10.5575/geosoc.115.288>
- Sciences, P. (1978). The mechanisms of creep in olivine. *Philosophical Transactions of the Royal Society of London - Series A: Mathematical and Physical Sciences*, 288(1350), 99–119. <https://doi.org/10.1098/rsta.1978.0008>
- Skemer, P., Katayama, I., Jiang, Z., & Karato, S. I. (2005). The misorientation index: Development of a new method for calculating the strength of lattice-preferred orientation. *Tectonophysics*, 411(1–4), 157–167. <https://doi.org/10.1016/j.tecto.2005.08.023>
- Skrotzki, W. (1994). Defect structure and deformation mechanisms in naturally deformed augite and enstatite. *Tectonophysics*, 229(1–2), 43–68. [https://doi.org/10.1016/0040-1951\(94\)90005-1](https://doi.org/10.1016/0040-1951(94)90005-1)
- Soustelle, V., & Manthilake, G. (2017). Deformation of olivine-orthopyroxene aggregates at high pressure and temperature: Implications for the seismic properties of the asthenosphere. *Tectonophysics*, 694, 385–399. <https://doi.org/10.1016/j.tecto.2016.11.020>
- Stocker, R. L., & Ashby, M. F. (1973). On the rheology of the upper mantle. *Reviews of Geophysics and Space Physics*, 11(2), 391–426. <https://doi.org/10.1029/rg011i002p00391>
- Stöffler, D., Hamann, C., & Metzler, K. (2018). Shock metamorphism of planetary silicate rocks and sediments: Proposal for an updated classification system. *Meteoritics & Planetary Sciences*, 53(1), 5–49. <https://doi.org/10.1111/maps.12912>
- Sundberg, M., & Cooper, R. F. (2008). Crystallographic preferred orientation produced by diffusional creep of harzburgite: Effects of chemical interactions among phases during plastic flow. *Journal of Geophysical Research*, 113(12), 1–16. <https://doi.org/10.1029/2008JB005618>
- Tasaka, M., Michibayashi, K., & Mainprice, D. (2008). B-type olivine fabrics developed in the fore-arc side of the mantle wedge along a subducting slab. *Earth and Planetary Science Letters*, 272(3–4), 747–757. <https://doi.org/10.1016/j.epsl.2008.06.014>
- Tedonkenfack, S. S. T., Puziewicz, J., Aulbach, S., Ntaflou, T., Kaczmarek, M. A., Matusiak-Malek, M., et al. (2021). Lithospheric mantle refertilization by DMM-derived melts beneath the Cameroon Volcanic Line—A case study of the Befang xenolith suite (Oku Volcanic Group, Cameroon). *Contributions to Mineralogy and Petrology*, 176(5), 1–18. <https://doi.org/10.1007/s00410-021-01796-3>
- Treiman, A. H. (2005). The nakhlite meteorites: Augite-rich igneous rocks from Mars. *Chemie Der Erde - Geochemistry*, 65(3), 203–270. <https://doi.org/10.1016/j.chemer.2005.01.004>
- Udry, A., & Day, J. M. D. (2018). 1.34 billion-year-old magmatism on Mars evaluated from the co-genetic nakhlite and chassignite meteorites. *Geochimica et Cosmochimica Acta*, 238, 292–315. <https://doi.org/10.1016/j.gca.2018.07.006>
- Udry, A., Howarth, G. H., Herd, C., Day, J. M. D., Lapen, T. J., & Filiberto, J. (2020). What martian meteorites reveal about the interior and surface of Mars. *Journal of Geophysical Research: Planets*, 125(12), e2020JE006523. <https://doi.org/10.1029/2020JE006523>
- Ulrich, S., & Mainprice, D. (2005). Does cation ordering in omphacite influence development of lattice-preferred orientation? *Journal of Structural Geology*, 27(3), 419–431. <https://doi.org/10.1016/j.jsg.2004.11.003>
- Van der Werf, T., Chatzaras, V., Marcel Kriegsman, L., Kronenberg, A., Tikoff, B., & Drury, M. R. (2017). Constraints on the rheology of the lower crust in a strike-slip plate boundary: Evidence from the San Quintín xenoliths, Baja California, Mexico. *Solid Earth*, 8(6), 1211–1239. <https://doi.org/10.5194/se-8-1211-2017>
- van Roermund, H. L. M., & Boland, J. N. (1981). The dislocation substructures of naturally deformed omphacites. *Tectonophysics*, 78(1–4), 403–418. [https://doi.org/10.1016/0040-1951\(81\)90022-6](https://doi.org/10.1016/0040-1951(81)90022-6)
- Vollmer, F. W. (1990). An application of eigenvalue methods to structural domain analysis. *Bulletin of the Geological Society of America*, 102(6), 786–791. [https://doi.org/10.1130/0016-7606\(1990\)102<0786:AAOEMT>2.3.CO;2](https://doi.org/10.1130/0016-7606(1990)102<0786:AAOEMT>2.3.CO;2)
- Watt, L. E., Bland, P. A., Prior, D. J., & Russell, S. S. (2006). Fabric analysis of Allende matrix using EBSD. *Meteoritics & Planetary Sciences*, 41(7), 989–1001. <https://doi.org/10.1111/j.1945-5100.2006.tb00499.x>
- Wenk, H.-R., & Tomé, C. N. (1999). Modeling dynamic recrystallization of olivine aggregates deformed in simple shear. *Journal of Geophysical Research*, 104(B11), 25513–25527. <https://doi.org/10.1029/1999jb900261>
- Winiarski, B., Gholinia, A., Mingard, K., Gee, M., Thompson, G., & Withers, P. J. (2021). Correction of artefacts associated with large area EBSD. *Ultramicroscopy*, 226(March), 113315. <https://doi.org/10.1016/j.ultramic.2021.113315>
- Woodward, C. (2005). Plasticity at the atomic scale: Parametric, atomistic, and electronic structure methods. *Handbook of Materials Modeling*, 2865–2869. https://doi.org/10.1007/978-1-4020-3286-8_171
- Yao, Z., Qin, K., Wang, Q., & Xue, S. (2019). Weak B-type olivine fabric induced by fast compaction of crystal mush in a crustal magma reservoir. *Journal of Geophysical Research: Solid Earth*, 124(4), 3530–3556. <https://doi.org/10.1029/2018JB016728>
- Zhang, J., & Green, H. W. (2007). Experimental investigation of eclogite rheology and its fabrics at high temperature and pressure. *Journal of Metamorphic Geology*, 25(2), 97–115. <https://doi.org/10.1111/j.1525-1314.2006.00684.x>
- Zhang, J., Green, H. W. II, & Bozhilov, K. N. (2006). Rheology of omphacite at high temperature and pressure and significance of its lattice preferred orientations. *Earth and Planetary Science Letters*, 246(3–4), 432–443. <https://doi.org/10.1016/j.epsl.2006.04.006>